



NLR-TP-2000-473

AIRcraft Drag And Thrust Analysis (AIRDATA)
Publishable synthesis report

M. Laban

This investigation has been carried out under a contract awarded by the European Commission, contract number BRPR-CT97-0470.

The European Commission and the contributing partners have granted NLR permission to publish this report.

The contents of this report may be cited on condition that full credit is given to NLR and the author.

| | |
|--------------------------|----------------|
| Division: | Fluid Dynamics |
| Issued: | June 2001 |
| Classification of title: | Unclassified |



SYNTHESIS REPORT FOR PUBLICATION

Contract No. : BRPR-CT97-0470
Project No. : BE97-4114
Title : AIRDATA

Coordinator : Nationaal Lucht- en Ruimtevaartlaboratorium (NLR)

| | | | |
|----------|---|--|----|
| Partners | : | Nationaal Lucht- en Ruimtevaartlaboratorium (NLR) | NL |
| | | Deutsches Zentrum für Luft- und Raumfahrt (DLR) | GE |
| | | Centro Italiano Ricerche Aerospaziali (CIRA) | IT |
| | | British Aerospace Sowerby Research Centre (BAe) | GB |
| | | Rolls-Royce (RR) | GB |
| | | Société de Construction des Avions Hurel-Dubois (HD) | FR |
| | | University of Naples "Frederico II" (UN) | IT |
| | | ANALYSIS Systems Research Hi-Tech SA (ASR) | GR |

Starting Date : 1-4-1998
Duration : 27 Month

Project funded by the European Community
under the Industrial and Materials Technologies
Programme (Brite-EuRam III)



This page is intentionally left blank.



Summary

Keywords: Engine/Airframe Integration, Thrust/Drag Bookkeeping, Drag Breakdown, CFD

0.1 Research Objectives, Key Results, and Exploitation Opportunities

The acronym AIRDATA stands for *AIR*craft *D*rag *A*nd *T*hrust *A*nalysis and the project forms part of a long term research strategy focusing on engine airframe integration studies funded by the European Union (DG-XII) and the participating organizations. The objective of the AIRDATA project is the development and validation of CFD-based tools for thrust, drag, and drag breakdown analysis of transport aircraft employing close-coupled high bypass ratio engines. The project addresses a number of technical issues which support this very challenging global project objective.

High accuracy of the computed flow field based on the Navier-Stokes equations is a prerequisite for accurate thrust and drag assessment. Therefore topics of engine flow modeling, turbulence models, and numerical schemes applied in the flow solvers are considered. Aerodynamic forces computed from CFD flow fields are sensitive to the size and quality of the computational meshes. Installation drag numbers with sufficient accuracy can only be obtained through grid optimization and application of procedures for aerodynamic force extrapolation to zero mesh size. Once good quality Navier-Stokes solutions are obtained on optimized grids, computation of thrust and drag coefficients is a non-trivial matter, as the straightforward approach of evaluating the pressure and friction integrals over the aircraft surface is not directly applicable to jet-powered configurations. Therefore, the momentum balance is used for thrust/drag bookkeeping in the project. For a deeper understanding of installation drag sources, a further breakdown of drag in vortex, wave, and viscous drag components is undertaken.

During the validation/demonstration phase of the project, the developed CFD tools are applied to the ALVAST model equipped with three different engine simulators and installation drag is computed. The numerical installation drag numbers are compared with the experimental results obtained during the ENIFAIR S1 measurement campaign. It is concluded that accurate installation drag assessment for wing-mounted jet engines is within reach of CFD today.

With the new CFD-based analysis capability in the loop, it would be feasible to optimize engine installations on future aircraft for minimal (engine interference) drag. It needs little imagination to estimate the impact of such a capability on the fuel burn of newly proposed long-range commercial transport aircraft if this opportunity would be exploited to its full extent by industry. Opportunities for the exploitation of the research carried out in AIRDATA are therefore enormous.



Contents

| | | |
|----------|--|-----------|
| 0.1 | Research Objectives, Key Results, and Exploitation Opportunities | 5 |
| 1 | Introduction | 9 |
| 1.1 | Need for an Accurate Engine Installation Drag Assessment Capability | 9 |
| 1.2 | CFD, a Complementary Approach to Wind Tunnel Testing for Engine Installation Drag Assessment | 9 |
| 1.3 | The AIRDATA Project | 9 |
| 1.4 | The AIRDATA Project Structure | 10 |
| 1.5 | Aim and Contents of this Report | 10 |
| 2 | Background on Engine Installation Drag | 11 |
| 2.1 | Definition of Engine Installation Drag | 11 |
| 2.2 | Breakdown of Engine Installation Drag | 11 |
| 2.3 | Required Accuracy of Engine Installation Drag Numbers | 12 |
| 3 | Flow Modeling for Thrust/Drag Analysis | 13 |
| 3.1 | Introduction | 13 |
| 3.2 | Engine Boundary Conditions | 13 |
| 3.3 | Turbulence Models | 14 |
| 4 | Grid Optimization and Aerodynamic Force Extrapolation | 16 |
| 4.1 | Introduction | 16 |
| 4.2 | Geometry Handling and Grid Generation | 16 |
| 4.3 | Grid Optimization | 17 |
| 4.4 | Local Grid Coarsening Techniques | 17 |
| 4.5 | Aerodynamic Force Extrapolation | 18 |
| 5 | Thrust/Drag Bookkeeping and Drag Breakdown Techniques | 20 |
| 5.1 | Introduction | 20 |
| 5.2 | Thrust/Drag Bookkeeping | 20 |
| 5.3 | Breakdown of Drag in Vortex, Wave, Viscous, and Spurious Components | 21 |
| 6 | Installation Drag Studies for the Three ENIFAIR Configurations | 23 |
| 6.1 | Introduction | 23 |



| | | |
|-----------|---|-----------|
| 6.2 | Analysis at the Design Point | 23 |
| 6.3 | Excursion in Lift Coefficient; Drag Polars | 25 |
| 6.4 | Excursion in Fan Pressure Ratio; Power Effects | 26 |
| 6.5 | Excursion in Mach Number; Transonic Drag Rise | 27 |
| 7 | Opportunities for Industrial Exploitation of the Project Results | 29 |
| 7.1 | Industrial Opportunities | 29 |
| 7.2 | Collaboration Sought | 29 |
| 7.3 | Publications | 30 |
| 8 | Conclusions and Outlook to the Future | 31 |
| 9 | Acknowledgements | 32 |
| 10 | References | 33 |

25 Figures



Nomenclature

Abbreviations

| | |
|---------|---------------------------------------|
| AIRDATA | AIRcraft Drag And Thrust Analysis |
| CFD | Computational Fluid Dynamics |
| DUPRIN | DUcted PROpfan INvestigations |
| ENIFAIR | ENgine Integration on Future AIRcraft |
| FPR | Fan Pressure Ratio |
| SOC | Start Of Cruise |
| TF | Turbo Fan |
| TFN | Through Flow Nacelle |
| TPS | Turbine Powered Simulator |
| UHBR | Ultra High Bypass Ratio |
| VHBR | Very High Bypass Ratio |

Symbols

| | |
|---------------|--|
| C_D | Dimensionless drag coefficient |
| C_L | Dimensionless lift coefficient |
| h | Relative mesh size |
| M | Mach number |
| M_∞ | Freestream Mach number |
| M_{dd} | Drag divergence Mach number |
| \bar{n} | Normal vector |
| R | Gas constant |
| Re | Reynolds number |
| V | Velocity |
| V_∞ | Freestream velocity |
| γ | Specific heats ratio |
| Δs | Entropy change relative to freestream condition |
| η | Dimensionless semispan location |
| ζ | Vorticity component parallel to freestream velocity vector |
| ψ | Streamfunction |
| Ω | Flow field domain |
| ρ | Density |
| ρ_∞ | Freestream density |



1 Introduction

1.1 Need for an Accurate Engine Installation Drag Assessment Capability

In response to a growing demand for environmentally friendly products and to rising long term prices of fuel, the world's major airlines feel compelled to introduce low-noise and fuel-efficient aircraft in their fleet. Driven by economical motives and constraint by low-noise requirements imposed by regulators, the engine manufactures improve the propulsive efficiency and reduce the noise level of their engines. The greatest potential for gaining engine propulsive efficiency is to increase the fan bypass ratio, Ref. 1. However, a higher bypass ratio leads to an increase of the external diameter of the engine in comparison with present-day turbofans. If the aircraft's sill heights and landing gear heights are not to be compromised too seriously, this leads to *close-coupled* wing-engine configuration with potential adverse interference effects on the wing aerodynamic performance, Ref. 2. The economical pay-off of installed high bypass ratio engines is positive if the increase in propulsive efficiency outweighs the associated higher nacelle and interference drag over the full range of aircraft operation. The environmental pay-off is already positive if new noise regulation standards can only be met with larger diameter engines even if the fan by-pass ratio is beyond the economical optimum value. To realize this, it is of utmost importance to identify, to comprehend, and to quantify the physical sources of engine installation drag.

1.2 CFD, a Complementary Approach to Wind Tunnel Testing for Engine Installation Drag Assessment

Quantifying engine installation drag has long remained the domain of wind tunnel testing. In the mean time, CFD has matured to such an extent that it can play a role in the optimization of jet-engine installations. Moreover, CFD can potentially provide a cost effective and complete physical understanding of aerodynamic efficiency losses which result from the installation of an engine to a wing. This detailed information on the mechanisms of aerodynamic efficiency losses is the key factor to success for configuration optimization.

1.3 The AIRDATA Project

Although the solution of the Navier-Stokes equations for the computation of the flow field around complete aircraft with installed jet-engines is at present more or less state-of-the-art, the use of this data to determine aerodynamic performance losses is not yet routinely performed. For this reason, a 2-year Brite Euram project named *AIRDATA* was launched on 1 April 1998, Ref. 3. The acronym *AIRDATA* stands for *AIRcraft Drag And Thrust Analysis* and the project forms part of a long term Brite Euram research strategy focusing on engine airframe integration studies initiated by the DUPRIN (Ref. 4) and ENIFAIR (Figures 1 through 3) projects.



1.4 The AIRDATA Project Structure

The main objective of the AIRDATA project is the development and validation of CFD-based tools for thrust, drag, and drag breakdown analysis of transport aircraft employing close-coupled high bypass ratio engines. This overall objective is broken down in a number of technical sub-objectives which are mapped to different tasks within the AIRDATA project (Ref. 3):

- AIRDATA Task 1: Project management.
- AIRDATA Task 2: Improved flow modeling for thrust/drag analysis.
- AIRDATA Task 3: CFD grid generation, grid optimization, and extrapolation of aerodynamic forces to zero mesh size.
- AIRDATA Task 4: Development of thrust, drag, and drag component breakdown diagnostics capabilities for computed flow fields based on the Navier-Stokes equations.
- AIRDATA Task 5: Demonstration of technology readiness through the provision of new (CFD based) knowledge on the physical sources of installation drag and installation drag numbers for the ENIFAIR configurations (DLR-ALVAST model equipped with three different engine simulators: TF, VHBR, and UHBR) at various flow conditions.
- AIRDATA Task 6: Exploitation issues.

1.5 Aim and Contents of this Report

A full description of the results from the AIRDATA project are collected in Refs. 5 and 6 as well as a number of internal reports and publications produced by the individual partners. The following chapters of this report provide a synthesis of the key project results.



2 Background on Engine Installation Drag

2.1 Definition of Engine Installation Drag

The total effect on drag due to installation of an underwing jet-engine is expressed by the term *Engine Installation Drag*. Engine installation drag is defined as the horizontal shift of the Wing/Body/Pylon/Nacelle drag polar versus the Wing/Body drag polar. Figure 4 illustrates this definition with an application to the ALVAST model equipped with a *Very High Bypass Ratio* (VHBR) engine simulator. ENIFAIR experimental results and AIRDATA numerical results are shown. The ENIFAIR experimental results are derived from semispan model force balance measurements in the ONERA S1 wind tunnel (Ref. 7) corrected for calibrated engine simulator thrust (Ref. 8).

2.2 Breakdown of Engine Installation Drag

Engine installation drag comprises four main contributions:

- The viscous drag of the nacelle.
Viscous boundary layer losses on the external nacelle duct is the major contributor to engine installation drag. Nacelle viscous drag is mainly a function of nacelle diameter and stream-wise nacelle length. Engine throttle setting (weakly) influences these viscous losses through modification of the outer nacelle pressure distribution. Characteristic nacelle viscous drag numbers are in the order of magnitude of 15 drag counts for a twin engined transport aircraft.
- The viscous drag of the pylon.
Viscous losses on the upper part of the pylon walls outside the fan jet contribute to drag (the lower part of the pylon walls inside the fan jet lay in the thrust domain). The pylon contributes a few counts to viscous drag.
- Engine interference on wing vortex drag.
The spanwise lift distribution over the wing changes due to the mounting of an engine. In most aircraft designs, the wing-alone features a triangular-shaped lift distribution for aerodynamic-structural optimization reasons. Engine interference on the wing lift distribution may results in a shift away from this optimized distribution, hence a few counts change in vortex drag.
- Engine interference on upper-wing wave drag.
Wing wave drag changes as a result of three factors. First, lift carry-over takes place to some extent from the wing to the nacelle. The decrease of wing lift yields an associated decrease in wing wave drag. Secondly, the above mentioned spanwise redistribution of the wing loading results in modified wing wave drag losses. Finally, the local nacelle-induced flow distortions on the wing will locally affect wing wave drag. The total contribution of



the three factors amount to a few counts change in wing wave drag with either positive or negative sign.

Relative simple engineering methods (e.g. flat plate theory) could be employed to assess, approximately, the viscous drag associated with the additional nacelle and pylon wetted surface. Unfortunately, no simple methods exist which can assess the more complicated effect of mutual nacelle/wing flow interference. In the transonic flight regime, even relative small disturbance of the flow over the wing may have relative large impacts on drag. This calls for the application of CFD-based techniques based on solving the Navier-Stokes equations.

2.3 Required Accuracy of Engine Installation Drag Numbers

Characteristic engine installation drag numbers for a twin-engined transport aircraft are 10 to 20 counts. Individual physical drag components, as listed in the previous section, can be as low as a single drag count. Viewed in this light, the required accuracy for the computation of engine installation drag and the individual installation drag components is also a single drag count. Due to imperfections in the currently applied turbulence models, single drag count absolute accuracy obtained from CFD calculations still presents an unresolved challenge. For engine installation drag, the approach is to extract these numbers from two different flow solutions (Wing/Body/Pylon/Nacelle minus Wing/Body), and errors due to turbulence model imperfections will cancel out to a certain extent. If the numerical flow solver errors and thrust/drag bookkeeping issues can be solved properly, the required single drag count engine installation drag accuracy may eventually be reached with CFD technology.



3 Flow Modeling for Thrust/Drag Analysis

3.1 Introduction

A prerequisite for accurate thrust/drag computations is the availability of high quality flow fields obtained from CFD computations. Topics of special interest for engine/airframe flow field computations are the applied turbulence model and the modeling of the engine exhaust jets.

3.2 Engine Boundary Conditions

Several CFD models can be selected to represent the engine flow field in installation drag studies. As the definition of drag excludes the engine flow domain itself (Section 5.2), the details of the internal engine flow field are not of direct interest. However, the way in which the engine flow interacts with the airframe flow does have an impact on installation drag.

Engine/airframe flow interaction upstream of the engine, over the outer-nacelle surface, and through the nacelle/pylon/lower-wing gully, are affected by the *engine mass flow ratio*. Engine/airframe flow interaction downstream of the engine is affected by the post-exit jet characteristics (jet-spreading and jet-entrainment).

A suitable single engine parameter related to the engine mass flow as well as the post-exit jet characteristics is the *Fan Pressure Ratio* (FPR). The Fan Pressure Ratio is defined as the ratio of the total pressure distribution averaged over the fan jet exhaust plane and the freestream static pressure. For the three engine simulators considered in project (TF, VHBR, UHBR), the engine operating conditions at the design point are:

| | |
|------|------------|
| TF | FPR = 2.33 |
| VHBR | FPR = 2.09 |
| UHBR | FPR = 1.72 |

In the current project, the fan and core jets are chosen to be modeled by domain inflow planes on which appropriate boundary conditions are enforced.

In the ONERA-S1 experiments, the engine simulators were equipped with a number of total pressure and total temperature rakes in the fan and core exits, Ref. 7. NLR, CIRA, and HD applied radially and circumferentially varying S1-measured total pressure distributions at their CFD exhaust planes, while DLR and BAe used radially varying but circumferentially-averaged distributions.



On the fan intake plane, all CFD methods applied a static pressure boundary condition which is controlled in such a way that the engine simulator's fan-inlet/fan-outlet mass flow equilibrium is obtained.

DLR, CIRA, and HD performed extensive studies in which the exhaust plane averaged total pressure profiles are evaluated against non-uniform profiles. Figure 5 shows an example.

DLR observed that the post-exit jet-spreading and jet-entrainment characteristics differ significantly for both types of boundary conditions and this influences the aerodynamic forces acting on the nacelle. This leads to the conclusion that the implementation of realistic non-uniform engine boundary conditions is a prerequisite for accurate engine installation drag computations.

3.3 Turbulence Models

Imperfections in the presently used turbulence models can cancel out to a certain extent in the computation of engine installation drag. What does not cancel out are details in the pylon, nacelle, and jet flows. For engine/airframe integration, the accurate prediction of dominant post-exit jet characteristics, such as spreading rate and entrainment, is a key issue. The ability to capture such effects correctly depends on the combination of an accurate modeling of the fan-jet starting conditions (Section 3.2) and on the applied turbulence model which affects the further downstream development of the fan jet and its mixing with the airframe flow. Another aspect of interest is the accurate simulation of corner flows which occur in the wing/pylon/nacelle junctions. Flow separations are frequently observed in these areas. Correct CFD detection ability of such phenomena is another key issue.

DLR evaluated the algebraic Baldwin-Lomax and the two equation k-omega turbulence models for fully turbulent flow, and flow with prescribed boundary layer transition location. The study was performed on the Wing/Body/TF configuration using the multiblock structured FLOWer code. Figure 6 presents details of the skin friction lines in the immediate surrounding of the pylon as computed by both turbulence models. The k-omega turbulence model computes flow separations at the pylon/nacelle and pylon/wing junctions, while the Baldwin-Lomax model computes fully attached flow at those locations. The Baldwin-Lomax model leads to higher lift and drag values ($\Delta C_L = 10\%$, $\Delta C_D = 5\%$) compared to the corresponding computations with the two-equation k-omega model.

HD evaluated three different turbulence models; the one-equation Spalart-Allmaras model (used in conjunction with wall-functions), and the two-equation Standard and Realizable k-epsilon mod-



els. Solutions are obtained on hybrid meshes using the FLUENT flow solver for the Wing/Body and Wing/Body/UHBR configurations. It is found that both k-epsilon models give highly similar results both in pressure distributions as well as in aerodynamic force coefficients. The solutions obtained with the Spalart-Allmaras model shows marked differences compared to the k-epsilon model results.



4 Grid Optimization and Aerodynamic Force Extrapolation

4.1 Introduction

Aerodynamic forces computed from CFD flow fields are critically sensitive to the size and quality of the computational meshes. A brute force approach, in which a given non-optimized grid is refined globally until the required numerical accuracy of the aerodynamic force coefficients is obtained (e.g. the required single drag count level as discussed in Section 2.3), will lead to a requirement on the number of grid cells which is beyond today's supercomputer capabilities. Accurate thrust/drag data can be obtained only through grid optimization in combination with procedures to extrapolate the aerodynamic forces to the limit of zero mesh size.

4.2 Geometry Handling and Grid Generation

Multiblock structured grids were generated by NLR using the domain modeler ENDOMO and grid generator ENGRID. The Wing/Body, Wing/Body/TF and Wing/Body/UHBR initial grids were inherited from ENIFAIR Task 5.3 activities, Ref. 9. In the course of the project, many geometrical details were added and/or corrected. The engine simulator outflow ducts were modeled more realistically (e.g. addition of the core plug) to allow for a correct engine mass flow simulation (Section 3.2). During the S1 test campaign, it turned out that the carbon fiber wing exhibits large flexibility with respect to bending and torsion. At the $M = 0.75$, $C_L = 0.50$, $Re = 4.3$ million design point, model tip rotations of about 1.6 degree were measured with an optical system. The outerwing geometry is corrected for this phenomenon according to a theoretical estimate of the spanwise wing twist distribution.

The set of multiblock structured grids was completed with the addition of the Wing/Body/VHBR configuration. All grids were further optimized to enable the computation of aerodynamic force coefficients with maximal accuracy (see Section 4.3). The final multiblock structured grids for each of the three installed configurations features 120 blocks and 4.5 million grid cells. Figure 7 shows the surface grid for the Wing/Body/TF configuration.

Parallel to this activity, Rolls Royce constructed fully unstructured grids for the Wing/Body and Wing/Body/VHBR configurations using the ICEM-CFD system. Prismatic grid elements are used in the boundary layer domain and tetrahedral grid elements in the outerflow domain.

Hurel Dubois constructed hybrid grids for the Wing/Body and Wing/Body/UHBR configurations. The grid features 2.86 million cells for the installed configuration. Block structured meshes are used in the viscous domains. Neighboring structured blocks are coupled by incorporation of lay-

ers with unstructured prism cells between the faces of adjacent structured blocks. Unstructured tetrahedral elements are employed in the inviscid outerflow domain. The density of the block-structured meshes in the boundary layers is adapted to the flow through local grid enrichment techniques such that suitable values for y^+ are obtained. Figure 8 shows the surface grid for the Wing/Body/UHBR configuration.

4.3 Grid Optimization

NLR investigated several strategies to identify grid anomalies which lead to unacceptable numerical errors in the computation of the flow field on the initial multiblock structured grids. The most effective technique appeared to be the concept of *spurious entropy drag*. Entropy along streamlines should remain at its constant freestream level as long as no dissipative processes such as for example shock waves or boundary layers are encountered. The spurious production or loss of entropy due to grid anomalies can be related to spurious drag through evaluation the integral expression (Ref. 11),

$$C_{D_{spur}} = \frac{2}{\gamma M_\infty^2} \int \left(\frac{\rho V}{\rho_\infty V_\infty} \right) \frac{\Delta s_{spur}}{R} \frac{dA}{S_{ref}} \quad (1)$$

along a line (2D) or plane (3D) perpendicular to the freestream flow (Δs is the entropy change relative to upstream infinity and R is the gas constant).

Guided by the concept of spurious entropy drag, the initial multiblock structured grids could be improved significantly. Figure 9 shows how the spurious production of entropy around the nacelle was reduced in this process. The optimized grids feature a 50 percent reduction in total spurious drag production in the inviscid outerflow domain relative to the initial grids from Ref. 9.

4.4 Local Grid Coarsening Techniques

Block-structured grid topologies frequently lead to regions in the flow field where high density of grid cells occur without physical need. DLR and CIRA investigated local grid coarsening techniques in which block to block coupling techniques are used with non-matching boundary techniques. Several grid coarsening strategies were tested. However, no single approach could be found that led to a significant saving in flow field computation time without sacrificing the accuracy of the aerodynamic forces.



4.5 Aerodynamic Force Extrapolation

For complex flow solver algorithms it is difficult to establish a stringent theoretical error estimate. This holds even for the specification of the order of error magnitude in terms of the grid cell size h . The block-structured Navier-Stokes codes used in the project are second order accurate in h , except at specific regions, such as shock waves, farfield boundaries, and non-smooth block-to-block connections, where the schemes degrade to first order accuracy. Hence, the overall algorithm features a mix of first and second order accuracy. Define $h = 1$ as a representative value for the cell size on the finest grid level. Then, it can be postulated that in some cell size range $0 < h < h_{max}$, the force coefficients computed on a sequence of nested grids are a function of the relative cell size parameter h according to one of the two equations,

$$C_D(h) = C_{D_{h=0}} + c_1 h + c_2 h^2 \quad (2)$$

$$C_D(h) = C_{D_{h=0}} + c_3 h^{(3/2)} \quad (3)$$

in which c_1 through c_3 denote constants and $C_{D_{h=0}}$ is the configuration drag coefficient at vanishing mesh size.

The strategy applied in grid refinement investigations is to solve the Navier-Stokes equations on a number of nested grids, and compute the corresponding drag coefficients, such that sufficient equations are obtained to calculate the constants in Equations 2 or 3. In order to determine the influence of the cell size h only, the required sequence of nested grids are best generated through successive grid coarsening (leading to $h = 2, h = 4, h = 8, \dots$) such that they feature constant characteristics in terms of the cell angles, cell aspect ratios, and cell stretchings. Equation 3 requires two grid levels ($h = 1, fine; h = 2, medium$), while Equation 2 requires an additional grid level ($h = 4, coarse$). Application of the latter strategy holds the risk that the main flow features, such as shock waves, are insufficiently resolved on the coarse grid level $h = 4$.

Figure 10 shows the drag results for the Wing/Body and Wing/Body/Pylon/Nacelle configurations at the nested grid levels and their extrapolated values to $h = 0$. As the approach to $h = 0$ is different for the Wing/Body/Pylon/Nacelle configurations relative to the Wing/Body configuration, directly comparing drag on the fine grid level for installation drag assessment yields biased results. Note that at $h = 0$, both NLR and DLR installation drag numbers for the TF and VHBR cases show excellent agreement, while this is not the case at the fine ($h = 1$) or medium ($h = 2$) grid levels.



It is concluded that a grid extrapolation procedure is essential for correct installation drag assessment on the currently used block-structured grids containing 4.5 million grid cells.



5 Thrust/Drag Bookkeeping and Drag Breakdown Techniques

5.1 Introduction

Once the Navier-Stokes equations are solved, thrust/drag analysis is a non-trivial matter. The classical approach is a rather straightforward evaluation of pressure and friction integrals over the aircraft surface ("near-field" approach). Yet, for powered configurations this does not directly lead to sensible drag numbers due to the presence of the fan and core jets which continue to expand behind the configuration (post-exit thrust).

For a deeper understanding of engine installation drag sources, it is enlightening to undertake a further breakdown of the drag component in *vortex drag* (associated with the generation of lift), *wave drag* (associated with the formation of shock waves), *viscous drag* (associated with the formation of boundary layers and shear layers) and *spurious drag* (associated with non-physical drag due to limited quality of the grid and numerical errors in the flow solver). Techniques to do so were insufficiently matured in the literature and are further developed within the project. Refs. 10, 11, 12, 13, 14 outline the development of the drag breakdown algorithms in more detail.

5.2 Thrust/Drag Bookkeeping

CFD-based thrust/drag bookkeeping is a topic tackled within the project by DLR. Thrust follows the definition of *Engine Net Thrust*, i.e. all momentum changes felt by the flow passing through the engine from far upstream (station 0) to far downstream (station e) are attributed to engine thrust, see Figure 11. All remaining forces are bookkept as airframe drag. The flow stagnation line on the nacelle intake highlight as well as the nacelle trailing edge separate the thrust from the drag domain. Surface pressure and friction integrals provide the basic thrust and drag components. Corrections are added for the pre-entry thrust (i.e. between stations 0 and i) and post-exit thrust (i.e. between stations o and e) components. The pre-entry thrust component can be computed as the far upstream flow conditions are known. The post-exit thrust component would require integrating the actual forces acting on the expanding jet. This rather complicated procedure can be circumvented by assuming the jet to expand isentropically and to use this assumption to predict the jet momentum at the required far downstream location (station e).

The thrust/drag bookkeeping algorithms are coded in the tool *AeroForce*, Ref. 15. *AeroForce* interfaces to the various Navier-Stokes flow solvers by reading in data on the surface of the configuration in TECPLOT format. Apart from thrust/drag bookkeeping, *AeroForce* features a detailed breakdown of the aerodynamic forces over the various airframe components.

5.3 Breakdown of Drag in Vortex, Wave, Viscous, and Spurious Components

For a deeper understanding of installation drag sources, it is enlightening to undertake a further breakdown of drag in vortex, wave, viscous, and spurious drag components. Existing techniques (Ref. 10) were insufficiently matured. To remedy these shortcomings, the University of Naples developed the underlying mathematical background, Refs. 11, 12, 13.

The first step consists of splitting total drag in a vortex and an entropy component. Vortex (or induced) drag is associated with the generation of lift and can be computed by observing the vorticity parallel to the freestream velocity vector on a so-called *Trefftz plane* S_t located at some distance behind the configuration. NLR implemented a vortex drag algorithm based on the vorticity (ζ) - streamfunction (ψ) formulation.

$$C_{D_{vortex}} = \int_{S_t} \frac{\psi}{V_\infty l_{ref}} \frac{\zeta}{V_\infty / l_{ref}} \frac{dS}{S_{ref}} \quad \text{where} \quad \nabla^2 \psi(s, t) = -\zeta(s, t) \quad (4)$$

Figure 12 shows an application to the Wing/Body/TF configuration. The nacelle trailing edge streamtube is used to separate the engine net thrust domain from the drag domain on the Trefftz plane.

The second step is the further breakdown of entropy drag in its wave, viscous, and spurious components by writing the entropy drag expression in divergence form such that it can be assessed in the flow field domain Ω on a grid cell by grid cell basis.

$$C_{D_{entropy}} = \frac{2}{\gamma M_\infty^2} \int_{\Omega} \bar{\nabla} \left[f \left(\frac{\Delta s}{R} \right) \frac{\rho}{\rho_\infty} \frac{\bar{V} \cdot \bar{n}}{V_\infty} \right] \frac{d\Omega}{S_{ref}}$$

$$f \left(\frac{\Delta s}{R} \right) = \frac{\Delta s}{R} + \frac{1 + (\gamma - 1) M_\infty^2}{2\gamma M_\infty^2} \left(\frac{\Delta s}{R} \right)^2 \quad (5)$$

Assignment to either wave, viscous, or spurious components is based on an automated zonal detection algorithm. A grid cell entropy production is assigned to wave drag if the value of a *shock sensor*, based on the local velocity vector and local pressure gradient, exceeds the threshold value for shock wave cells. Figure 13 shows an application to UHBR installation wave drag assessment where the entropy increase is visualized on grid cells which pass the shock sensor test.



A grid cell entropy production is assigned to viscous drag if the value of a *viscous sensor*, based on the dissipation function associated with the total (fluid + eddy) viscosity, exceeds the threshold value for boundary layer and wake cells. Figure 14 shows an application to the Wing/Body configuration where the entropy increase is visualized in the flow around the wing on those grid cells which pass the viscous sensor test.

If neither the shock or the viscous sensor is activated, the entropy production is assigned to spurious (or non-physical) drag. Spurious drag is not added to the total drag balance and in this way the contribution of numerical errors resulting from the flow solver in the outer flow domain is left out. This presents a complementary approach to the grid extrapolation technique outlined in Section 4.5. The following table presents nearfield versus farfield drag balance results for the Wing/Body configuration at the design condition ($M = 0.75$, $CL = 0.50$, $Re = 4.3M$, S1-transition) obtained from Navier-Stokes flow fields produced with two different flow solvers (ENSOLV and ZEN) and two different turbulence models (k-omega and Spallart-Allmaras):

| | $C_{D_{vortex}}$ | $C_{D_{wave}}$ | $C_{D_{viscous}}$ | $C_{D_{farfield}}$ | $C_{D_{h=0}}$ | $C_{D_{h=1}}$ |
|------|------------------|----------------|-------------------|--------------------|---------------|---------------|
| NLR | 89 | 4 | 143 | 236 | 253 | 285 |
| CIRA | 87 | 4 | 188 | 279 | 282 | 304 |

CIRA and NLR jointly coded the vortex, wave, viscous, and spurious drag classification algorithm into the code *AIRDRAG*, Ref. 14. *AIRDRAG* interfaces to the various block-structured, unstructured, and hybrid flow solvers by reading in the data (state vector) of the 3D flow field in TECPLOT format.

6 Installation Drag Studies for the Three ENIFAIR Configurations

6.1 Introduction

The developed CFD-based thrust/drag analysis capability for jet-powered configurations is demonstrated through analyzing the ENIFAIR configurations Wing/Body/-TF/-VHBR/-UHBR at design as well as off-design conditions. The off-design conditions comprise lift coefficient, engine power setting, and Mach number departures from the design point. The ENIFAIR S1 wind tunnel data base (Ref. 7) is employed as a reference. Ref. 16 presents the results from these studies in more detail.

6.2 Analysis at the Design Point

The semispan ALVAST model in the ONERA-S1 wind tunnel, with engine simulators operating under *Start of Cruise* (SOC) conditions, is selected as the design point,

$$\begin{aligned}
 Mach &= 0.75 \\
 C_L &= 0.50 \\
 Re &= 4.30 \text{ Million} \\
 FPR &= 2.33/2.09/1.72 \quad \text{for TF/VHBR/UHBR} \\
 x/c_{transition} &= 0.05 \quad (\text{winglower}) \\
 x/c_{transition} &= 0.15 \quad (\text{wingupper}) \\
 x_{transition} &= 45 \text{ mm} \quad (\text{body}) \\
 x_{transition} &= 28 \text{ mm} \quad (\text{nacelle})
 \end{aligned}$$

Figure 15 shows the chordwise pressures distribution over the wing at a station inboard ($\eta = 0.330$) of the pylon for the three installed configurations and the Wing/Body configuration. CFD results and S1 results are presented. The computed effect of different engine installations on the wing upper-surface pressure distributions correlate well with the experimental results. The correlation between computed and measured wing lower-surface pressure distributions is less satisfactory. The Wing/Body/UHBR lower-wing/inboard-ylon experimental pressure distribution indicates a flow separation which is under-rated by the computations.



The computed engine installation drag counts at the design point are (NLR and DLR results with grid extrapolation, HD results for fine grid):

| | | TF | VHBR | UHBR |
|-----|----------------|----|------|------|
| S1 | W/T experiment | 14 | 13 | 13 |
| NLR | h=0, Eq. 2 | 14 | 12 | 17 |
| DLR | h=0, Eq. 3 | 16 | 13 | |
| HD | h=1 | | | 67 |

The computed TF and VHBR installation drag counts correlate very well with S1 experimental values when grid extrapolation techniques (Section 4.5) are applied to the results obtained from block-structured flow solvers. This correlation is unresolved for the UHBR. These observations should be seen in light of suspicions of incorrect TF and UHBR nacelle lip geometries in the computations, and a non-converging UHBR core flow in the computations due to the occurrence of massive flow separations in the diverging core exhaust duct. HD's hybrid grid result for the UHBR most likely suffers from spurious drag effects which are not compensated for by grid extrapolation techniques.

The computed engine installation vortex and wave drag counts at the design point are:

| | TF | VHBR | UHBR |
|-------------------------|----|------|------|
| $\Delta C_{D_{vortex}}$ | -2 | -3 | -2 |
| $\Delta C_{D_{wave}}$ | +2 | 0 | +1 |

Engine interference on the wing lift distribution results in an increased outwing loading (closer to the elliptical distribution), hence a few counts reduction in vortex drag.

As the nacelle diameters and wetted areas increase from the TF via the VHBR to the UHBR, one would expect the magnitude of the installation drag coefficients to be ordered in that way as well (i.e. the lowest numbers for the TF and the highest for the UHBR). Yet, the relative favorable effect of the VHBR installation on wing vortex and wing wave drag causes the VHBR installation drag to be among the lowest of the three engines considered.



6.3 Excursion in Lift Coefficient; Drag Polars

An important indicator for the aerodynamic performance of an aircraft is the drag polar,

$$C_D = f(C_L) \quad (6)$$

at constant Mach number, constant Reynolds number, and constant fan pressure ratio.

As outlined in Section 2.1, the first step in engine installation drag assessment is to construct the Wing/Body drag polar. Figure 16 shows the Wing/Body drag polar computed with different Navier-Stokes flow solvers at the fine grid level and force balance results obtained from S1 semi-span model experiments. Considerable scatter is observed in the computational results. The unstructured and hybrid flow solvers overrate drag compared to the results from the block-structured flow solvers at the same lift coefficient. Additionally, grid extrapolated drag polars are shown for the block-structured NLR and CIRA results. All block-structured results feature lower drag compared to the experimental results. This holds even to a greater extent for the grid extrapolated results. However, it should be recognized that, in general, force balance measurements on a semi-span wind tunnel model do not yield reliable aerodynamic forces due to tunnel wall interference effects.

The second step in engine installation drag assessment comprises the computation of the flow field for the installed configurations. Figure 17 shows the Wing/Body/VHBR wing chordwise pressure distributions just inboard and outboard of the pylon for three lift coefficients ($C_L=0.35/0.50/0.60$). Both computational and experimental results are presented. It is concluded that the computed trend with increasing lift coefficient correlates well with S1 experimental results.

Figure 18 shows the installation drag polars for all three engine types, computed as the "horizontal shift" in the Wing/Body/Pylon/Nacelle versus Wing/Body drag polars, i.e. the drag increment due to engine installation at constant lift. The grid extrapolated ($h=0$) installation drag polar for the VHBR engine correlates very well with the experimental data. The experimental data is derived from total force measurements with a force balance in the ONERA-S1 wind tunnel corrected for TPS thrust calibrated at the ONERA-S4B engine calibration facility (Refs. 7 and 8). Possible explanations for the unresolved correlations for the TF and UHBR engines were given in Section 6.2.



6.4 Excursion in Fan Pressure Ratio; Power Effects

The dependency of configuration drag on engine throttle setting is minimized due to the applied concept of *engine net thrust* in the thrust/drag bookkeeping procedure (Section 5.2). This concept implies that variations in pre-entry jet forces and post-exit jet expansion forces due to throttle setting variations belong to the thrust domain rather than the drag domain. However, a small degree of dependency of drag on throttle setting will remain.

To investigate the dependency of installation drag on engine throttle setting, additional flow computations are carried out with the engine simulators running under *Through Flow Nacelle* (TFN) condition at $M = 0.75$ and $C_L = 0.50$. At $M = 0.75$, this results in a fan pressure ratio of $FPR = 1.46$. Figure 19 shows DLR's FLOWer results of local Mach numbers in a vertical cutting plane through the centre of the installed TF engine simulator for both TFN and SOC conditions.

One of the main contributing factors to the dependency of installation drag on throttle setting is the viscous flow over the outer nacelle surface. Figure 20 shows NLR's ENSOLV results and S1 measurements with respect to the change in chordwise pressure distribution at three nacelle circumferential stations when proceeding from TFN to SOC condition for the Wing/Body/VHBR configuration. The viscous flow over the nacelle surface experiences higher adverse pressure gradients at TFN condition due to the smaller fan mass flow ratio, hence higher viscous drag losses on the nacelle at TFN conditions.

Downstream of the engine, the jet-velocities, jet-entrainment, and jet-spreading rates are a function of the fan pressure ratio. Figure 21 illustrates how this affects the pressure distribution on the pylon and lower-wing for the Wing/Body/VHBR configuration according to NLR's ENSOLV computations. The flow experiences higher streamwise pressure gradients at the SOC condition along the wing lower side and inboard-ptylon, hence higher viscous drag occurs in this region at the SOC condition.

Figure 22 shows the Wing/Body/VHBR wing chordwise pressure distributions just inboard and outboard of the pylon at the TFN and SOC conditions. Both computational and experimental results are presented. It is concluded that the computed trend with increasing fan pressure ratio correlates well with S1 experimental results.

Figure 23 summarizes the NLR, DLR, and HD numerical drag results versus S1 experimental data, derived from force balance measurements and TPS thrust calibrations. This table gives drag



results and computes the effect fan pressure ratio on installation drag (*power effect*: $C_D(SOC) - C_D(TFN)$).

Power effect on installation drag receives positive and negative contributions. The overall result is generally a small number which amounts to only a few counts. The computational results obtained with block-structured flow solvers in combination with grid extrapolation techniques correlate reasonable well for the VHBR engine. This correlation remains unresolved for the TF engine. The incorrect computational TF nacelle lip geometry causes strong outer-nacelle flow separations at the TFN condition, hence additional drag at this condition, hence a large negative power effect on installation drag. The S1-measured TF nacelle pressure distributions show no sign of such phenomena on the experimental nacelle geometry. HD's results for the power effect on installation drag for the UHBR again most likely suffers from uncompensated spurious drag effects.

6.5 Excursion in Mach Number; Transonic Drag Rise

Flow compressibility causes drag to rise with increasing freestream Mach number. Starting from low Mach numbers, drag initially rises slowly until shock waves appear. Increasing the Mach number beyond this point results in an exponential growth of drag, ultimately leading to wing buffet due to unsteady separated boundary layers at the shock foot location.

Transonic drag rise is defined as the drag increment relative to a low Mach number condition (typically Mach=0.50 or Mach=0.60),

$$\Delta C_{D_{transonic}} = C_D(M) - C_D(M = 0.60) \quad (7)$$

at constant lift coefficient, constant Reynolds number, and an appropriate choice of the fan pressure ratio as function of Mach number.

The upper limit to the economical Mach operational range for an aircraft is given by the drag divergence Mach number M_{dd} . A commonly used definition of M_{dd} is the value of the freestream Mach number for which holds,

$$\frac{\partial C_D}{\partial M}(M_{dd}) = 0.10 \quad (8)$$



Figure 24 shows the Wing/Body/VHBR wing chordwise pressure distributions just inboard and outboard of the pylon for three freestream Mach numbers ($M=0.60/0.70/0.75$). CFD results and S1 results are presented. Apart from irregular pressure distributions near the boundary layer transition location at $M=0.60$, it is concluded that the computed trend with increasing freestream Mach number correlates well with S1 experimental data.

Figure 25 shows NLR's ENSOLV fine grid ($h=1$) results for the Wing/Body and Wing/Body/VHBR configuration transonic drag rise relative to the $M=0.60$ condition as well as S1 experimental data. Both configurations feature nearly equal drag rise at the $M=0.70$ and $M=0.75$ conditions. Note that the computed drag rise is about half of the S1 measured drag rise. The S1 measurements, however, have been performed using a semispan model for which Mach dependent tunnel wall interference effects cannot be ruled out (a tunnel wall induced incidence effect of 0.1 degree would already explain the differences between semispan experimental data and the CFD results). The drag rise computations for the Wing/Body configuration have been extended to higher freestream Mach numbers. Wing/Body drag divergence occurs at $M_{dd} = 0.795$.

The presented results show that transonic drag rise is computed consistently for installed configurations. Unfortunately, experimental data are not available in the more interesting Mach number range where drag divergence occurs.

7 Opportunities for Industrial Exploitation of the Project Results

7.1 Industrial Opportunities

Aircraft manufacturers are currently mounting high bypass ratio engines on new aircraft products (e.g. Airbus A380). First applications of VHBR engine installations are found on long-range transport aircraft where gains in aerodynamic lift over drag performance have a more severe impact on the overall aircraft economical and environmental performance (e.g. Boeing 777 and Airbus A340-600). In this process, CFD is already used extensively during the design loop to check quantitative features of the flow field to ensure acceptable operation of the installed engine prior to its first flight (Ref. 18 provides a recent overview of procedures followed in this respect during the development of the A340-600). However, the drag penalties of a new engine mounting do become apparent only during the wind tunnel testing phase. At this stage, optimization of the design for minimum drag comes too late and is hardly feasible with a time consuming wind tunnel test campaign in the loop. As a result, the whole fleet of aircraft is burning more fuel than necessary over its entire life span.

Research in AIRDATA demonstrated that engine installation drag differences for different engine mountings can amount up to 5 drag counts in magnitude for currently designed commercial transport aircraft (i.e. 2 percent of the total aircraft drag at flight Reynolds numbers). Most of the differences originate from the mutual nacelle and wing flow interference which is not accessible to predictions with simple engineering methods. This margin (2 percent) can be seen as indicative for the savings that could potentially be realized when a high-fidelity CFD-based methodology for engine installation drag predictions would be available during the design optimization process.

The AIRDATA project set the first step in that direction, i.e. to deliver a CFD-based engine installation drag assessment capability. With this new analysis capability in the loop, industry would be able to really optimize new engine installations for minimal (engine interference) drag. Potential saving: 2 percent in drag during transonic cruise flight. It needs little imagination to estimate the impact of such a capability on the fuel burn of newly proposed long-range commercial transport aircraft.

7.2 Collaboration Sought

The AIRDATA project was executed in close collaboration with the ENIFAIR project, with which it was running in parallel. E.g. experimental ONERA S1 results obtained in the course of the ENIFAIR project (Ref. 7), were used extensively for comparison with CFD results obtained in the AIRDATA project (Chapter 6).



7.3 Publications

Key results obtained in the AIRDATA project have already been and will be disseminated further through the open-literature. Refs. 12, 13, 16, 17, 19, 20 provide examples.



8 Conclusions and Outlook to the Future

The AIRDATA project demonstrated that the required single drag count accuracy of computed engine installation drag numbers is within reach of CFD today. On the one hand, this is due to the development of methods for the computation of the aerodynamic forces from CFD flow fields and, on the other hand, due to recent developments on the CFD methods themselves. The latter relates to new advanced turbulence models which increase the accuracy of the computed flow field in the nacelle/pylon/jet region. Besides, supercomputers grew an order of magnitude in processing power since the start of the AIRDATA project. Instead of the applied multiblock structured meshes with 4.5 million grid cells, much more refined grids featuring 10 to 100 million grid cells would be feasible already today. This will lead to less spurious drag production, hence to much more accurate installation drag numbers.

As the main objective of AIRDATA is quite ambitious, it is not surprising that after 27 months of research a number of topics on the computation of engine installation drag are not completely concluded. Thrust/drag bookkeeping and drag breakdown methodology, as implemented in the developed postprocessing codes AeroForce and AIRDRAG, need consolidation. The applicability of a recently developed theory for the computation of viscous drag for jet-powered configurations has only scarcely been investigated in the limited term of the project. A follow-up research project on those items is therefore urgently needed.

Once single drag count accurate engine installation drag numbers can be quantified reliably with CFD, the potential for industrial application will be enormous. CFD will then be able to play a role in optimizing VHBR engine installations on long-range transport aircraft where gains in aerodynamic lift over drag performance have a direct impact on the overall aircraft economical and environmental performance. The AIRDATA project provided a big step forward in this respect with first-time engine installation drag numbers extracted from Navier-Stokes computed flow fields.



9 Acknowledgements

NLR would like to thank the participating institutions (NLR, DLR, CIRA, BAe, Rolls Royce, Hurel Dubois, University of Naples, and ANALYSIS Systems Research Hi-Tech) who carried out the research and contributed to results shown in this report. The following table lists the AIRDATA contact persons of each organization;

| Company | Name | Tel/Fax | Email |
|---------|---------------|---------------------|----------------------------------|
| NLR | M. Laban | +31-205113460/3210 | laban@nlr.nl |
| DLR | H. von Geyr | +49-5312952445/2320 | heiko.vgeyr@dlr.de |
| CIRA | L. Paparone | +39-823623345/3335 | l.paperone@cira.it |
| BAe | H. Figueiredo | +44-1179363009/3733 | hector.figueiredo@baesystems.com |
| RR | A. Smith | +44-1332249289/9513 | angus.smith@rolls-royce.com |
| HD | L. Devito | +33-146011060/1200 | laurent.devito@hureldubois.com |
| UN | R. Tognaccini | +39-817682179/2187 | rtogna@unina.it |
| ASR | A. Karidis | +30-17216272/7019 | karydis@asr.gr |

10 References

1. K. Rud and H.J. Lichfuss. *Trends in Aero-Engines Development*, Presented at: Aspects of Engine-Airframe integration for Transport Aircraft, DLR, 1996.
2. D.L. Berry. *The Boeing 777 Engine/Airframe Integration Aerodynamics Design Process*, ICAS 94-6.4.4, 1994.
3. NLR. *AIRCRAFT Drag And Thrust Analysis, Project Programme*, Annex I to Contract BRPR-CT97-470, 1997.
4. W. Burgsmueller, H. Hoheisel and J. Kooi. *Engine/Airframe Interference on Transport Aircraft with Ducted Propfans - The European Research Program DUPRIN*, ICAS-Paper 94-6.2.1, 1994.
5. M. Laban. *AIRCRAFT Drag And Thrust Analysis (AIRDATA), Final Report*, NLR-TR-2001-249, 2001.
6. M. Laban. *AIRCRAFT Drag And Thrust Analysis (AIRDATA), Exploitation Report*, NLR-TR-2001-225, 2001.
7. ONERA. *Tests on the ALVAST half model equipped with TPS6402, VHBR2, and CRUF2 powered nacelles in test section no 1-40 m² of SIMA wind tunnel*, Test Report, TR 2/8055 DSMA/Y, 1999.
8. ONERA. *Calibration of TPS6402, VHBR2, and CRUF2 Nacelles in the ONERA S4B Calibration Facility December 1997 to February 1998 Study No. 8055 GY 500G*, Test Report, PV 1/8055 DTEX/Y, 1998.
9. ONERA. *Calculation of Viscous Flow around Cruise Configuration (Subtask 5.3)*, ONERA Report RT 71/3271 DAAP/Y, 2000.
10. P. Iannelli, R. Tognaccini, *Drag prediction from CFD calculations: state of the art*, Technical Report of the Dipartimento di Progettazione Aeronautica, Universita degli Studi di Napoli, NT 98-34, 1998.
11. A. Pascarelli and R. Tognaccini. *Drag and Thrust Bookkeeping from CFD Calculations*, Technical Report of the Dipartimento di Progettazione Aeronautica, Universita degli Studi di Napoli, NT 00-43-2000.
12. R. Tognaccini and L. Paparone. *Drag Breakdown and Drag/Thrust Bookkeeping from CFD Calculations*, Workshop on European Research on Aerodynamic Engine/Airframe Integration for Transport Aircraft, Paper 10, Braunschweig, 2000.
13. L. Paparone and R. Tognaccini. *Computation and Breakdown of Drag in Viscous and Wave Components*, Submitted for publication: Journal of Aircraft, 2001.
14. C.M. van Beek, S.P. Spekreijse, and L. Paparone. *Description of Theory and User's Guide of AIRDRAG: A Computer Code for the Computation of Vortex, Viscous and Wave Drag of Airplane Configurations*, NLR Technical Report, NLR-TR-2001-241, 2001.

15. J. Wild. *AeroForce: Thrust Drag Bookkeeping and Aerodynamic Force Breakdown over Components*, DLR Technical Report, IB 129-99/9, 1999.
16. H. von Geyr. *Key Results of Detailed Thrust and Drag Studies on the ALVAST Configuration*, Workshop on European Research on Aerodynamic Engine/Airframe Integration for Transport Aircraft, Paper 12, Braunschweig, 2000.
17. M. Laban. *AIRCRAFT Drag And Thrust Analysis (AIRDATA) Project Overview and Key Results*, Workshop on European Research on Aerodynamic Engine/Airframe Integration for Transport Aircraft, Paper 9, Braunschweig, 2000.
18. A. Hurez. *Recent Progress on Engine/Airframe Integration on Airbus*, Presented at: Aeronautics Days 2001, January 2001, Hamburg.
19. M. Laban. *AIRDATA: CFD-Based Drag Analysis for Engine/Airframe Integration*, Presented at: Aeronautics Days 2001, January 2001, Hamburg.
20. H. von Geyr, O. Broderson, S. Melber. *Engine Integration on Transport Aircraft, The European Research Activities on Propulsion Airframe Integration*, To be presented at: Eccomas Computational Fluid Dynamics Conference, Swansea, 2001.

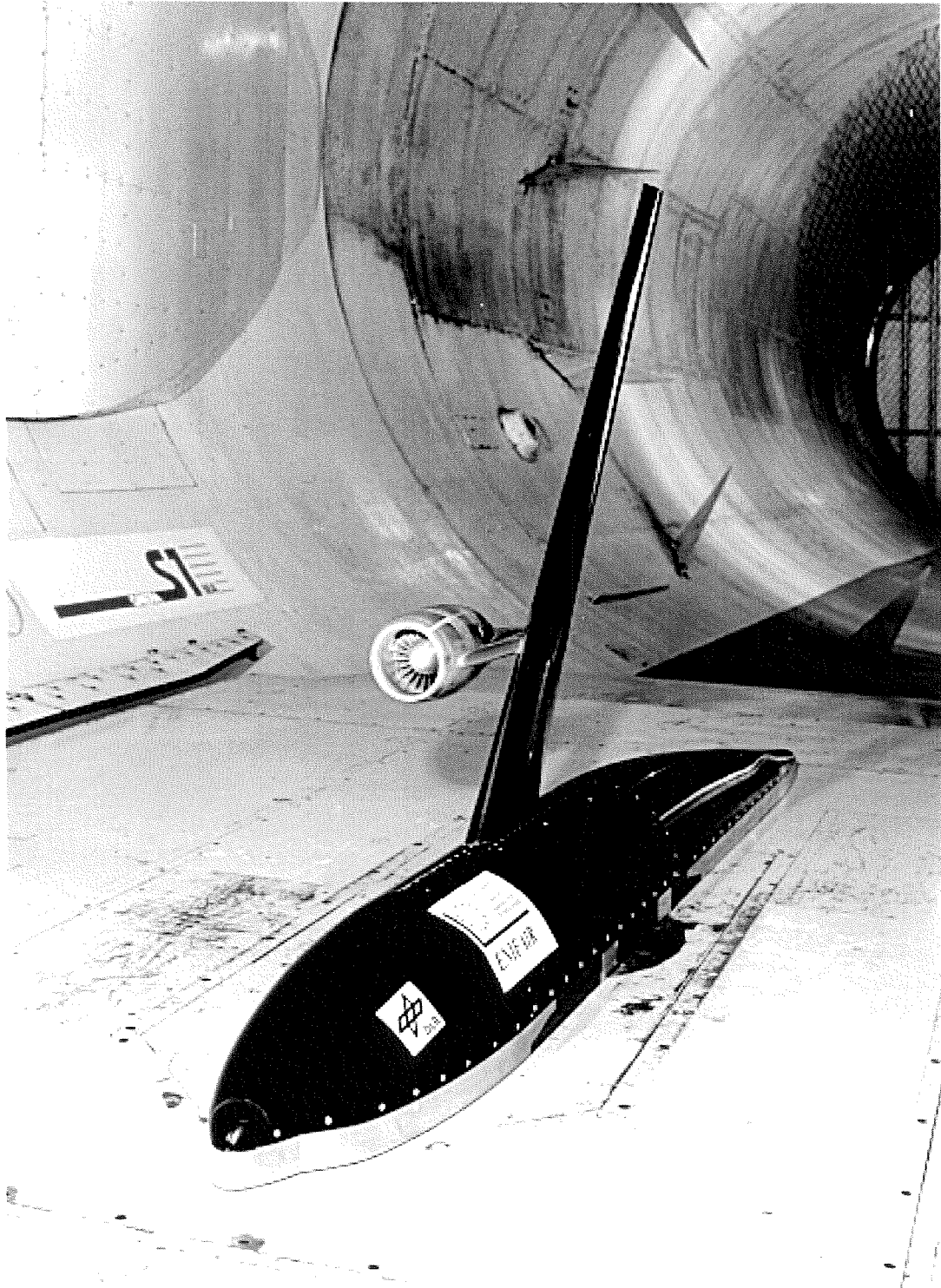


Fig. 1 The ALVAST semispan model equipped with the Turbo Fan (TF) engine simulator in the ONERA-S1 wind tunnel during the ENIFAIR measurement campaign.



Fig. 2 The ALVAST semispan model equipped with the Very High Bypass Ratio (VHBR) engine simulator in the ONERA-S1 wind tunnel during the ENIFAIR measurement campaign.

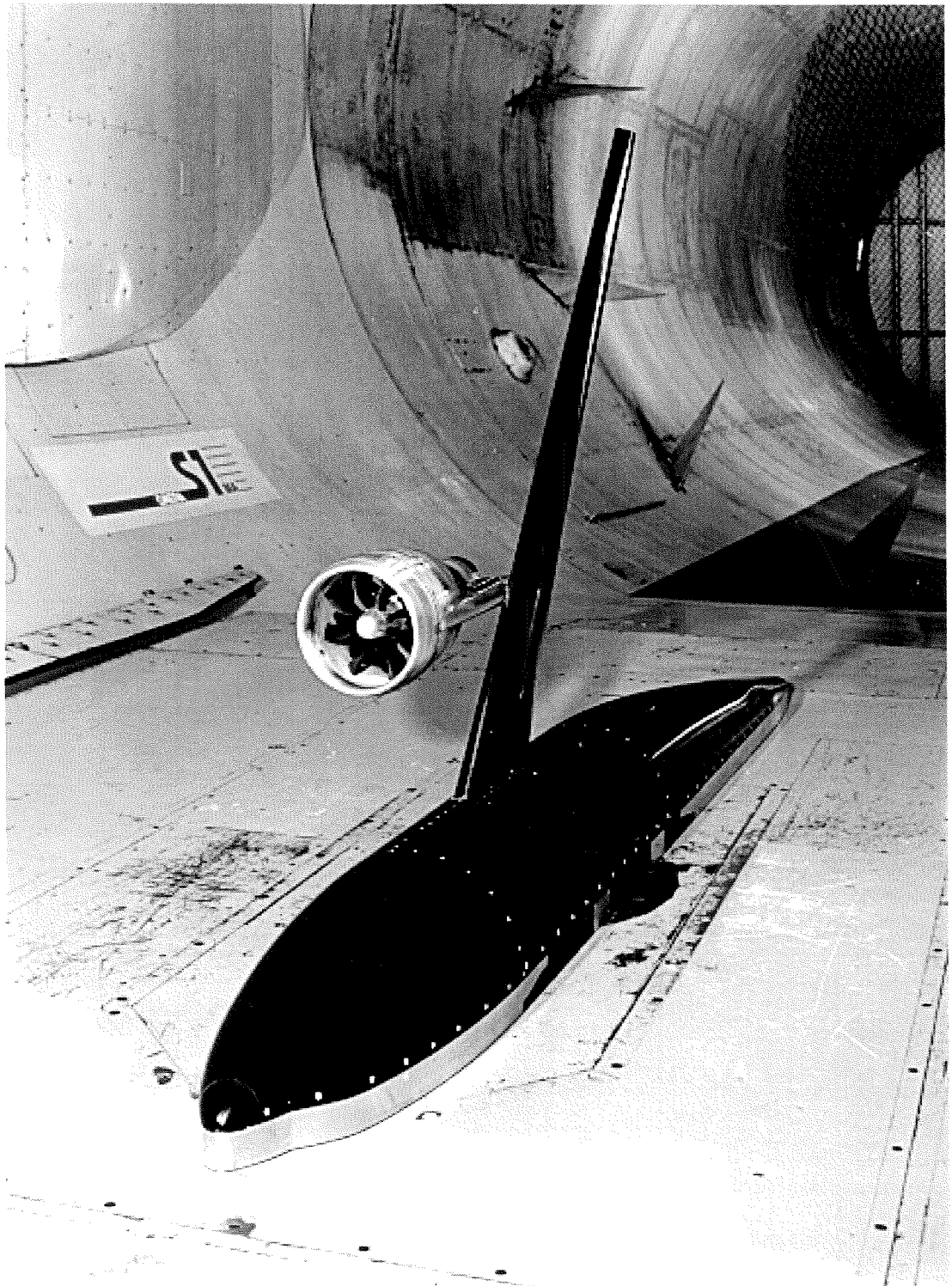


Fig. 3 The ALVAST semispan model equipped with the Ultra High Bypass Ratio (UHBR) engine simulator in the ONERA-S1 wind tunnel during the ENIFAIR measurement campaign.

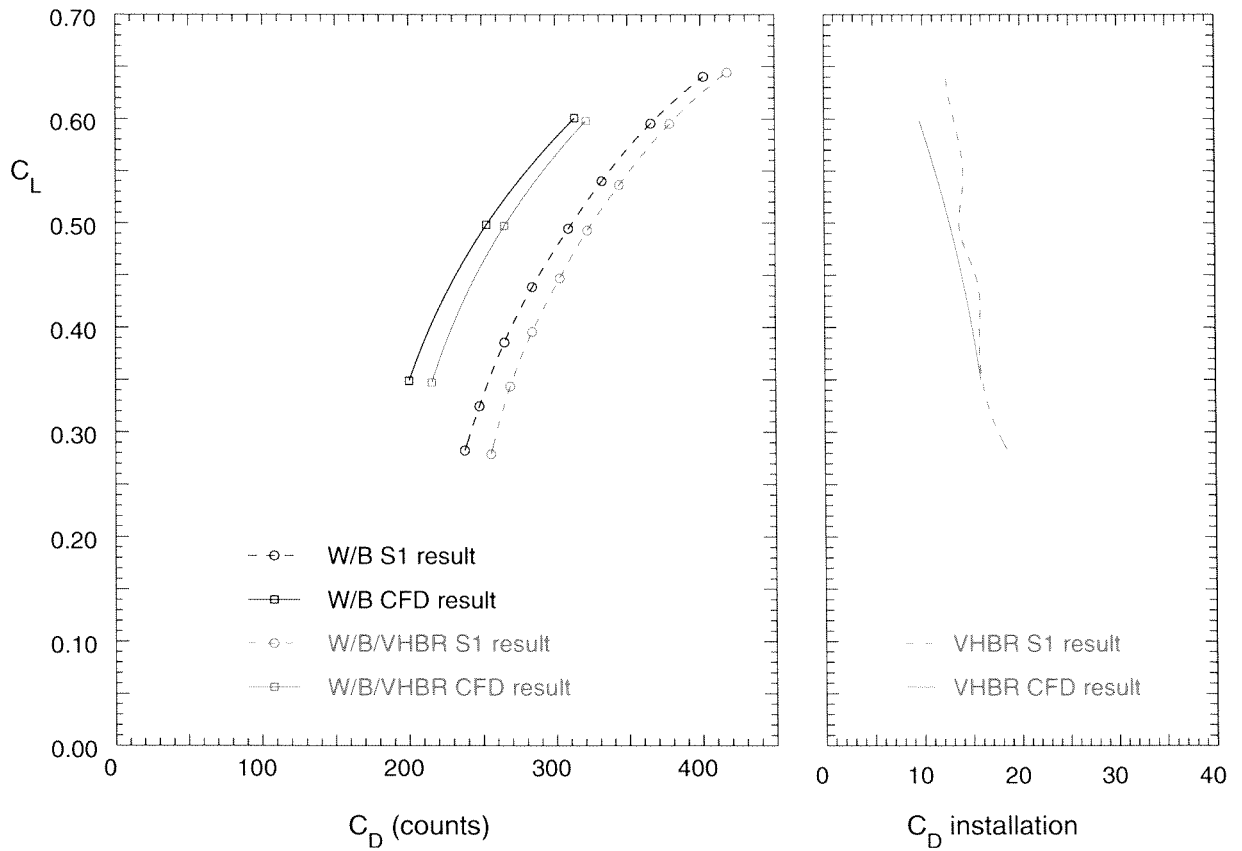


Fig. 4 VHBR engine installation drag counts computed as the horizontal shift in the W/B/VHBR drag polar versus the W/B drag polar (Mach=0.75, FPR=2.09, Re=4.3M, S1-transition). AIRDATA CFD results and ENIFAIR S1 experimental results (derived from semispan model force balance measurements and calibrated engine simulator thrust measurements) are shown.

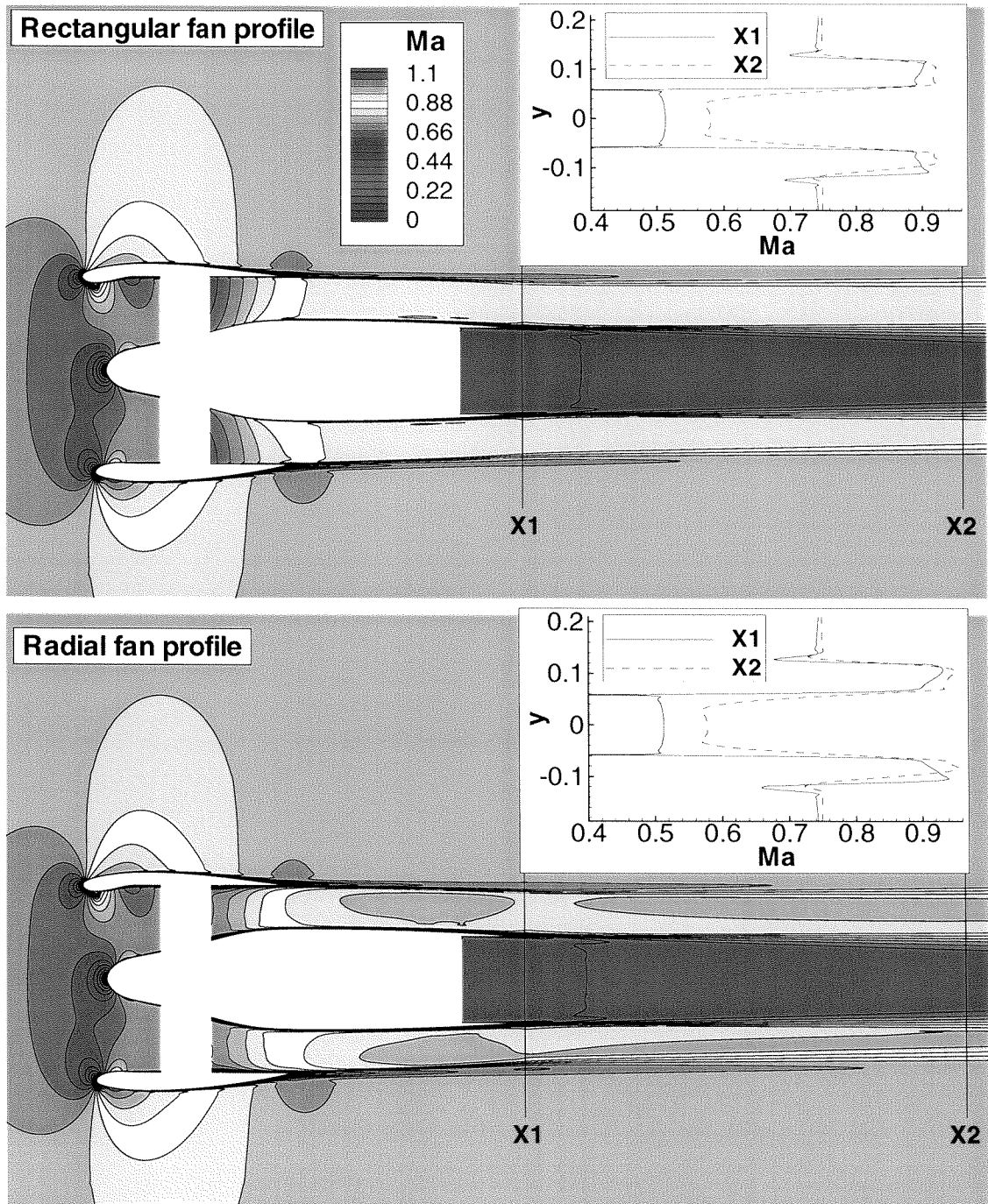


Fig. 5 The influence of exhaust plane averaged versus radially varying engine boundary conditions on the flow field computed around the isolated UHBR engine simulator.

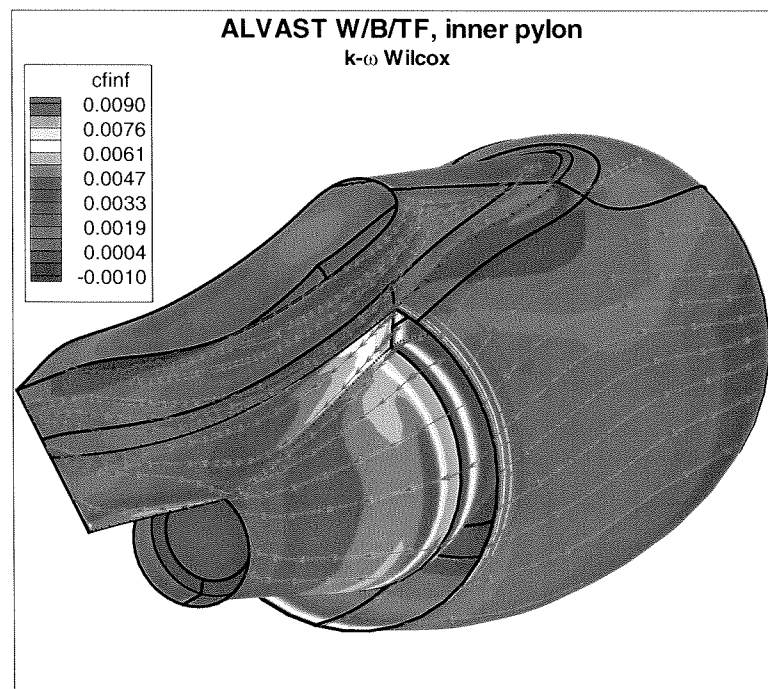
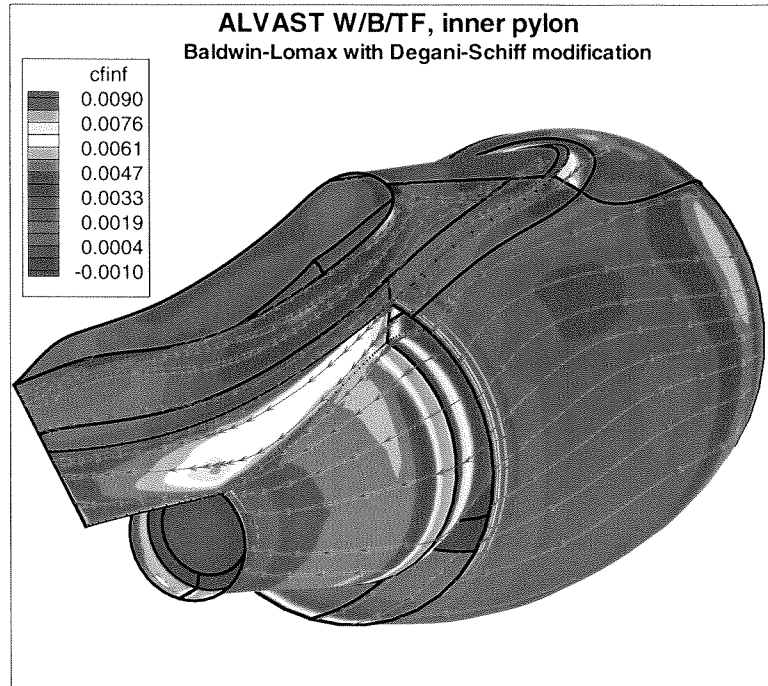


Fig. 6 Effect of different turbulence models on viscous flow over the pylon and the TF nacelle.

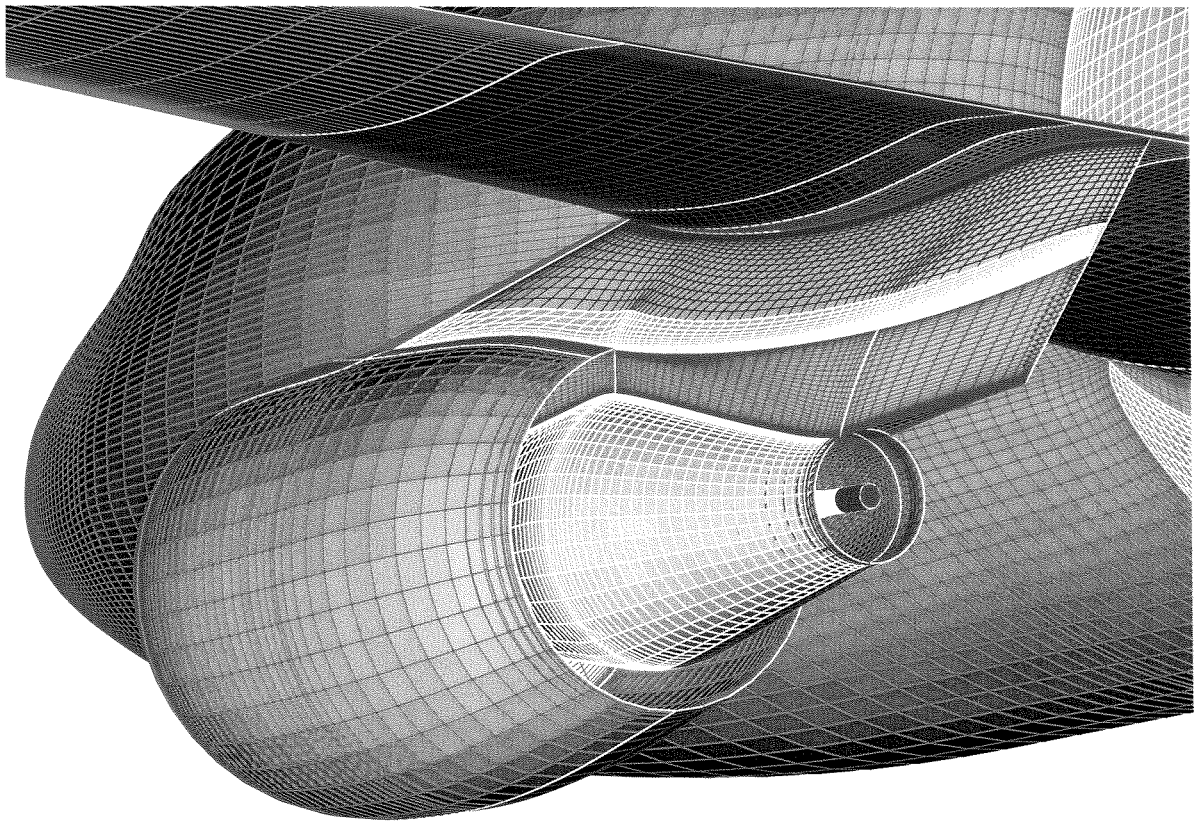


Fig. 7 Multiblock grid, Wing/Body/TF.

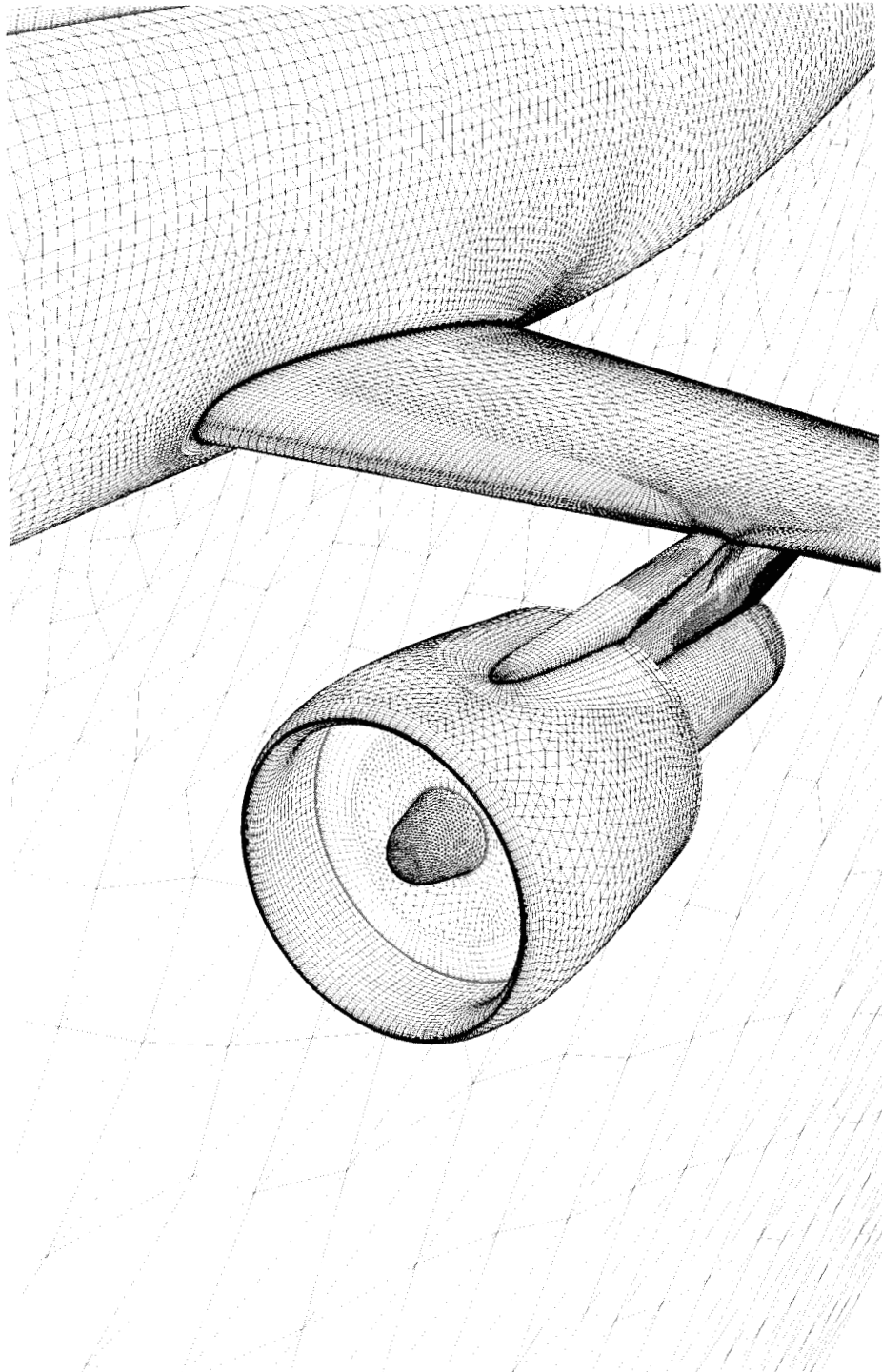


Fig. 8 Hybrid grid, Wing/Body/UHBR.

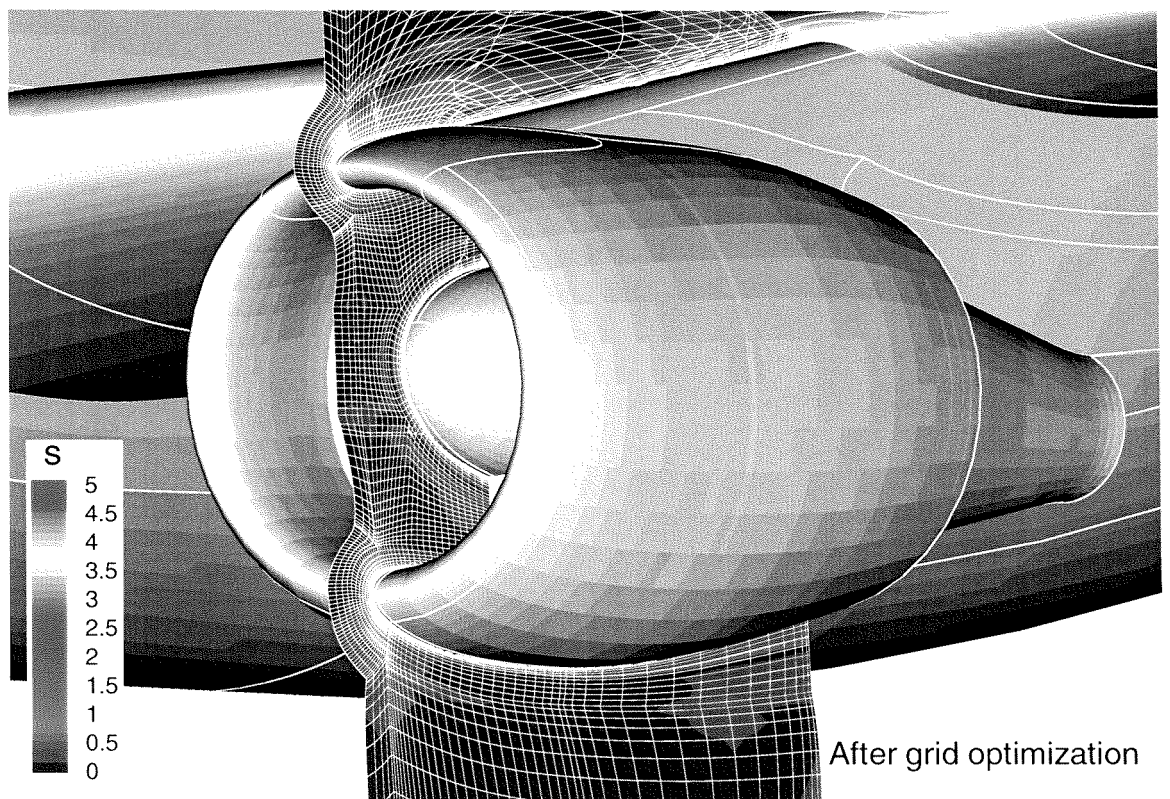
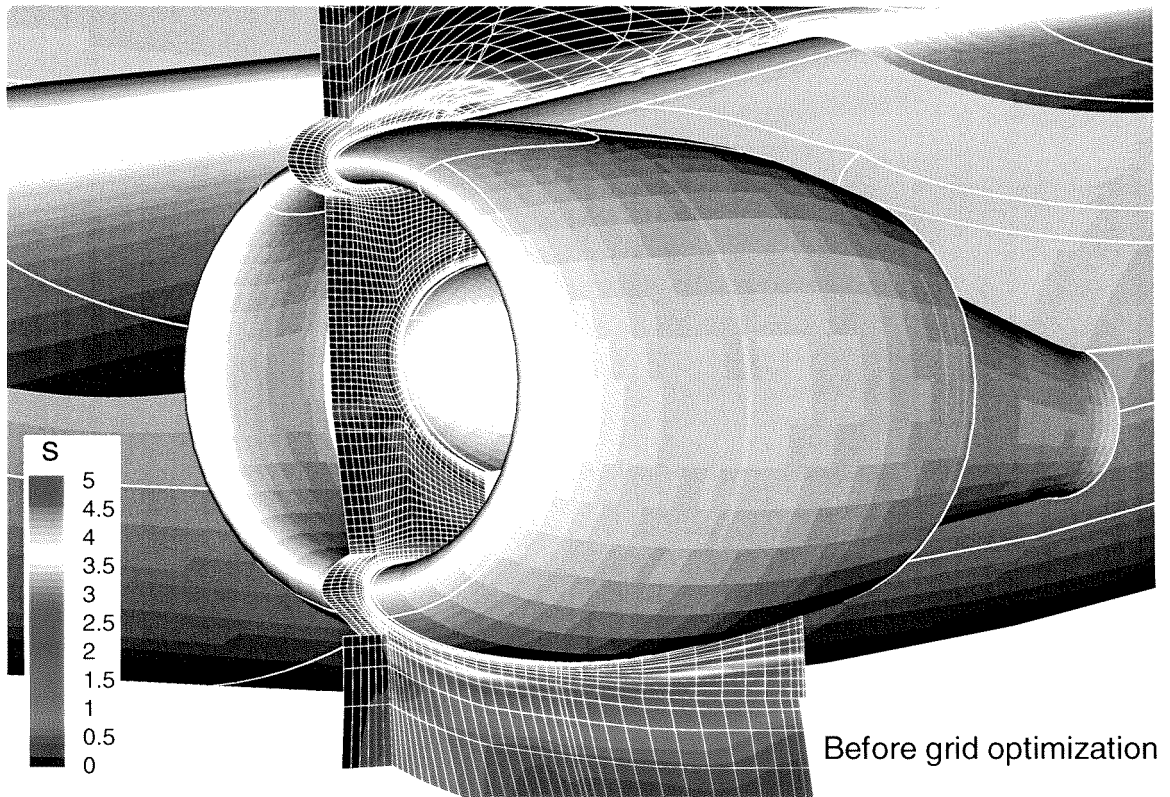


Fig. 9 Spurious production of entropy around the nacelle as indicator of grid quality, Wing/Body/TF (Mach=0.75, CL=0.50, FPR=2.33, Re=4.3M).

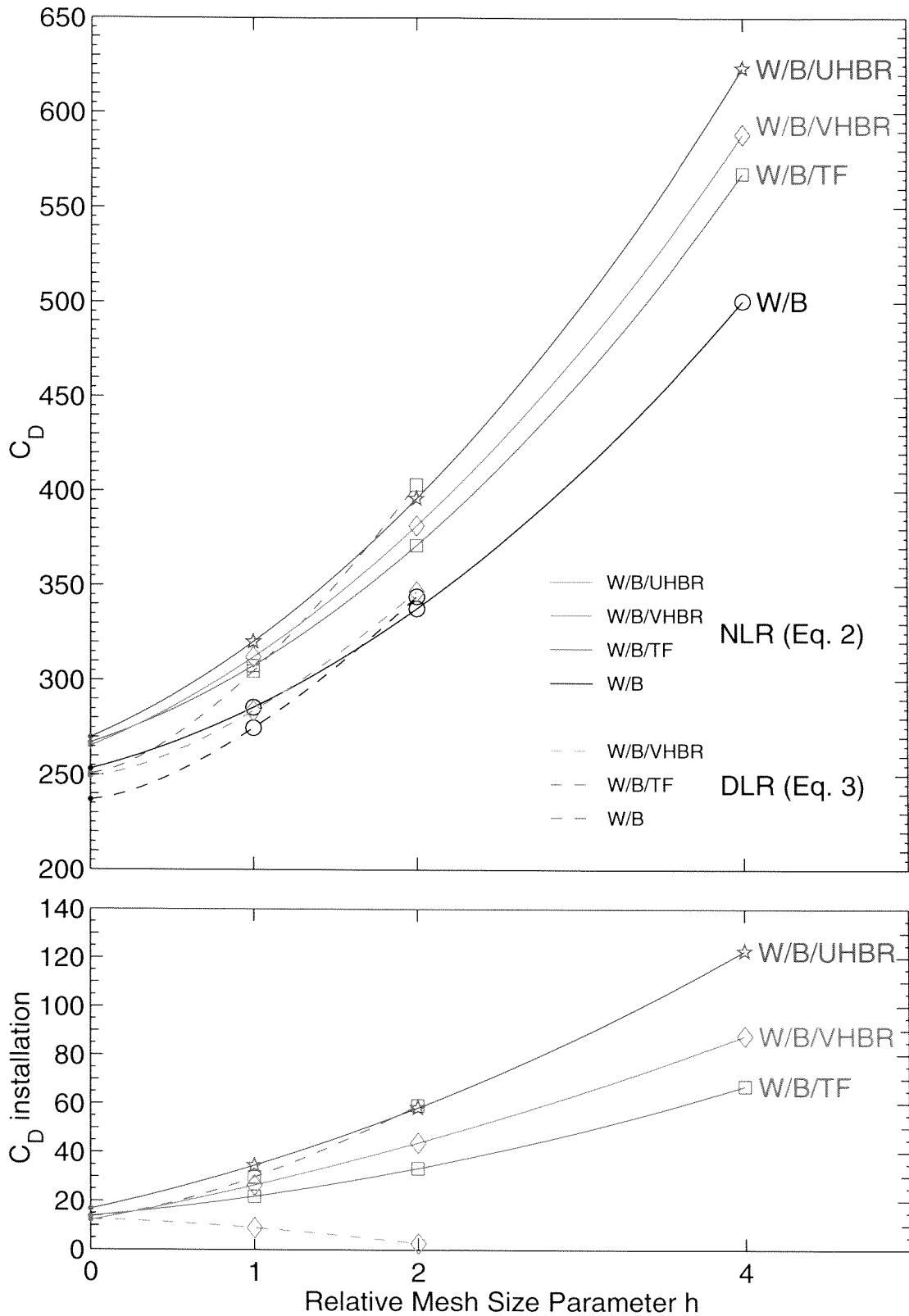


Fig. 10 Effect of aerodynamic force extrapolation on drag and engine installation drag (Mach=0.75, CL=0.50, FPR=2.33/2.09/1.72, Re=4.3M, S1-transition).

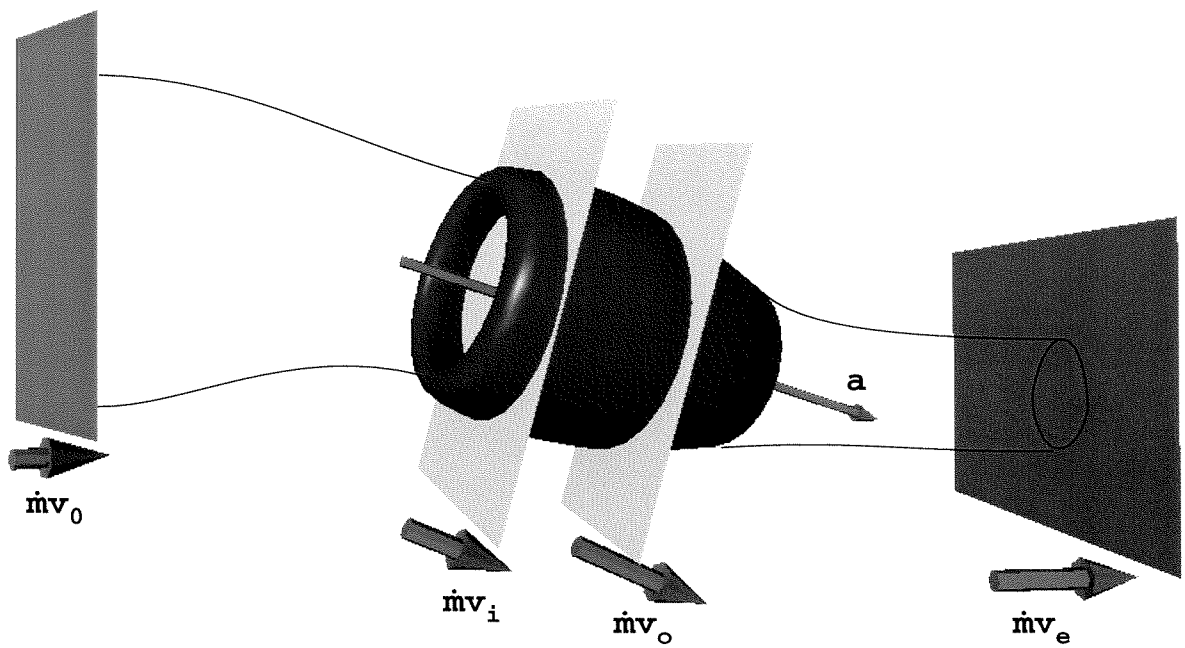
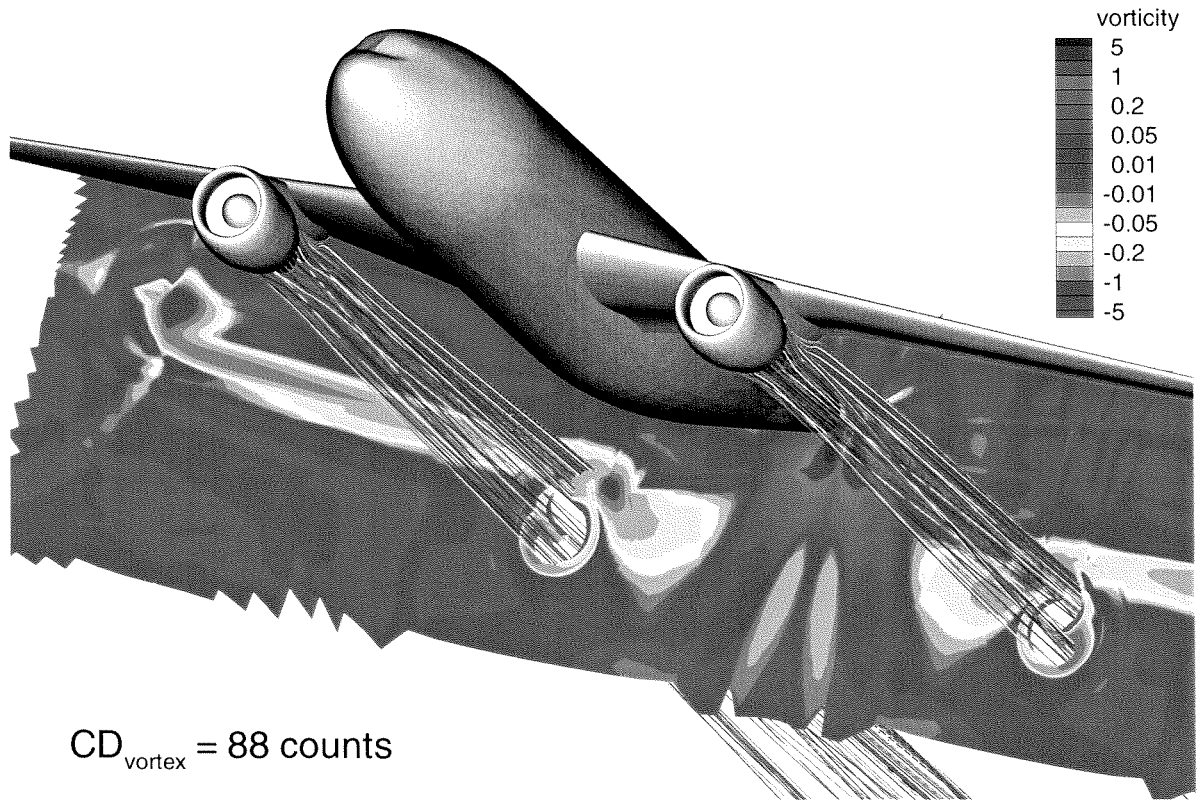


Fig. 11 Definition of Engine Net Thrust.



$CD_{vortex} = 88 \text{ counts}$

Fig. 12 Vortex drag evaluation on the Trefftz plane, Wing/Body/TF (Mach=0.75, $CL=0.50$, FPR=2.33, $Re=4.3M$, S1-transition)

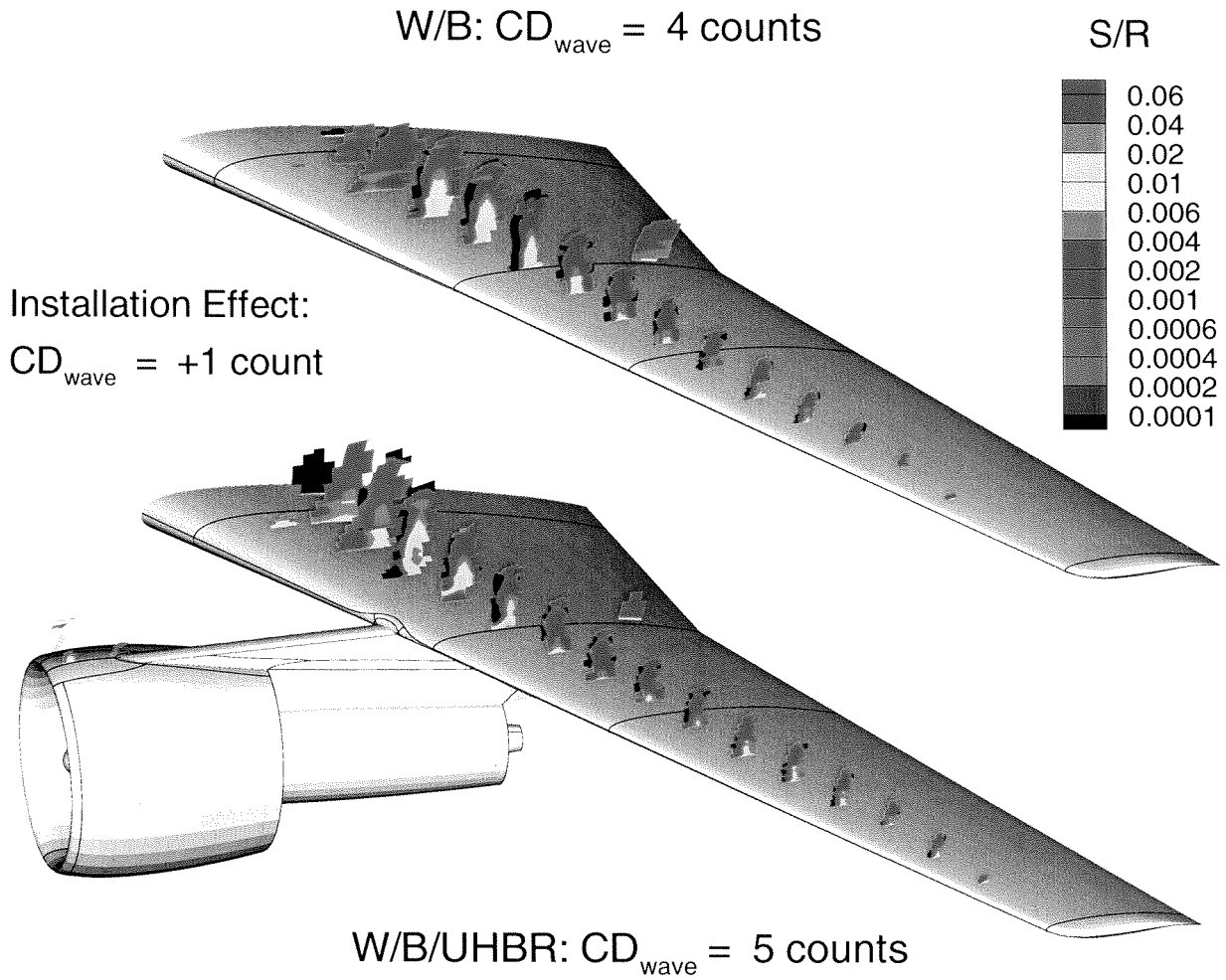


Fig. 13 Wave drag extracted from grid cell entropy production in shock region. Effect of UHBR engine installation on wave drag (Mach=0.75, $CL=0.50$, $FPR=1.72$, $Re=4.3M$, $S1$ -transition).

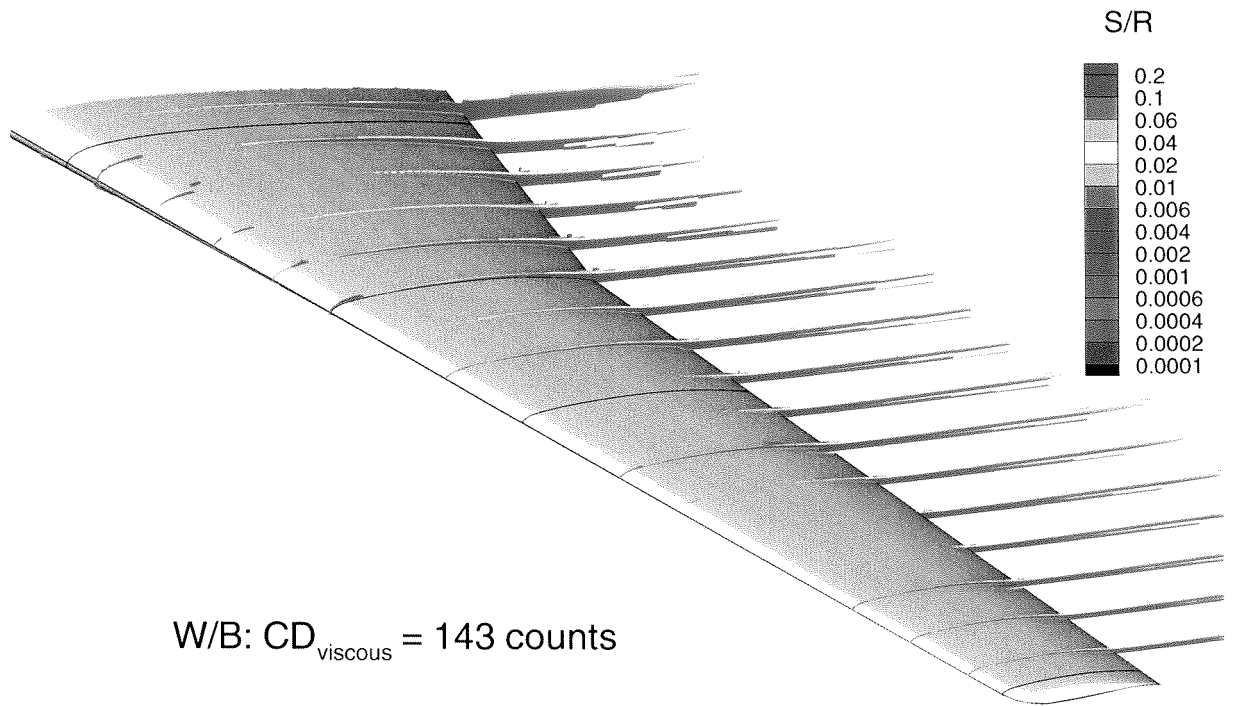


Fig. 12 Viscous drag extracted from grid cell entropy production in viscous region, Wing/Body (Mach=0.75, CL=0.50, Re=4.3M, S1-transition).

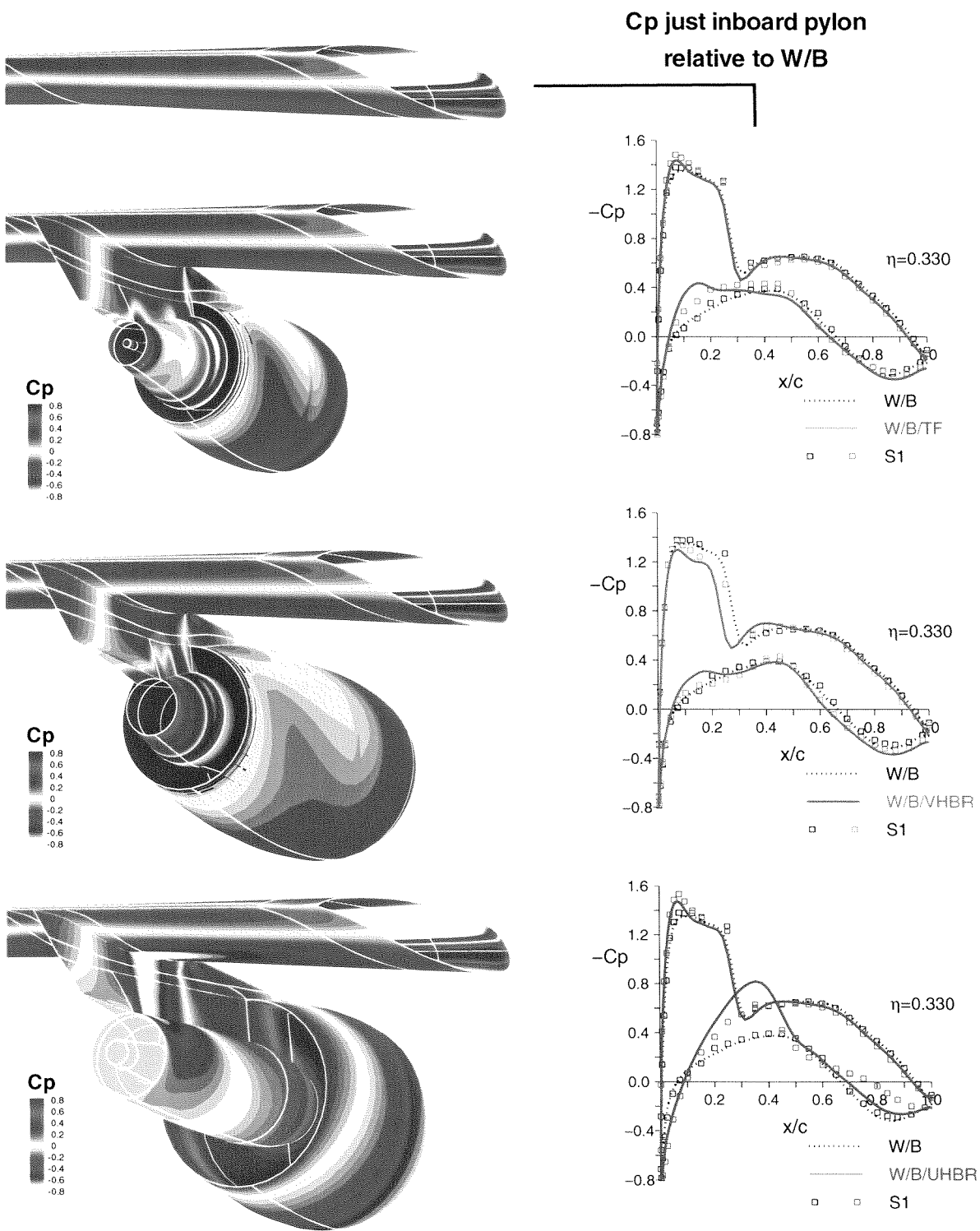


Fig. 13 Influence of different engine installations on wing pressure distribution ($Mach=0.75$, $CL=0.50$, $FPR=2.33/2.09/1.72$, $Re=4.3M$, $S1$ -transition).

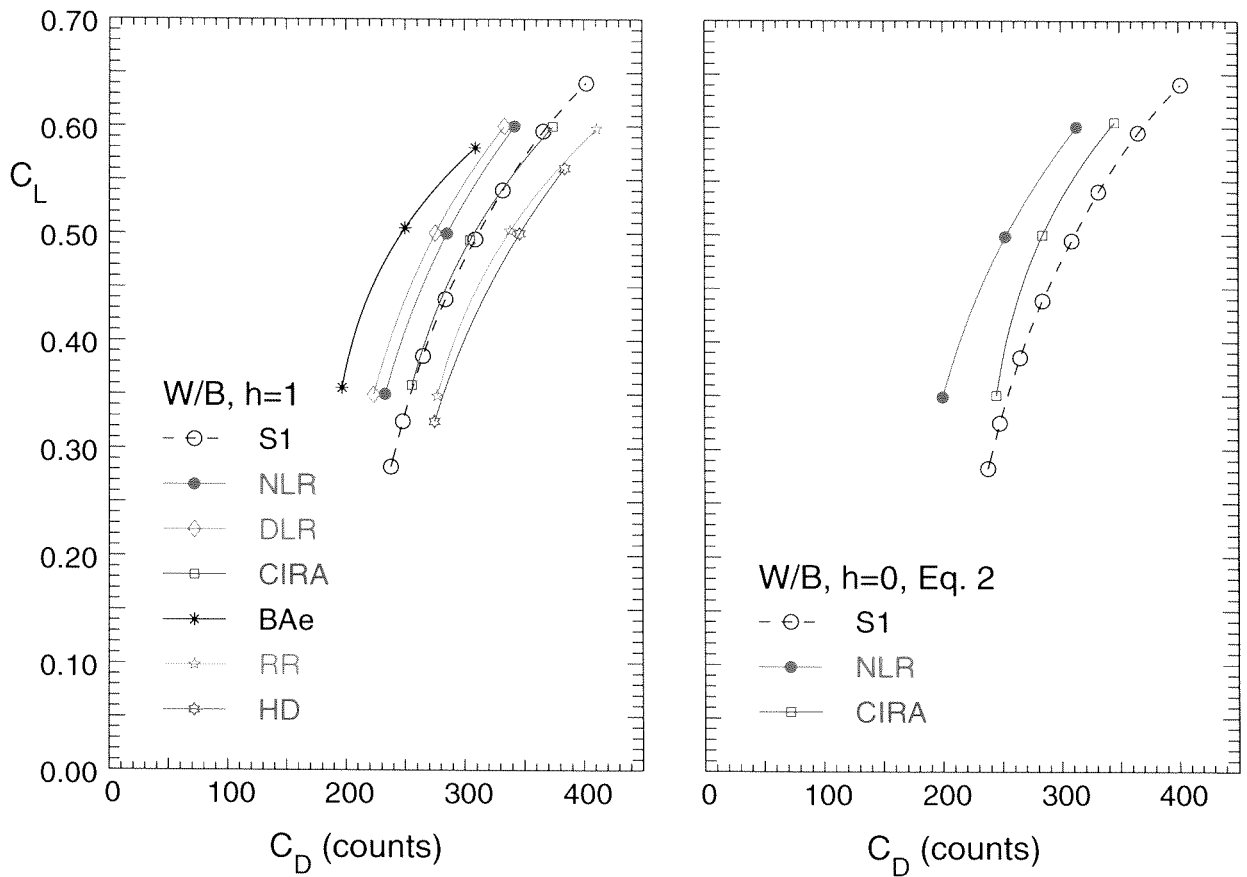


Fig. 14 Wing/Body drag polars computed by different flow solvers, fine grid and Eq. 2 grid extrapolated results (Mach=0.75, Re=4.3M, S1-transition for NLR, DLR, CIRA, fully turbulent for BAe, RR, HD).

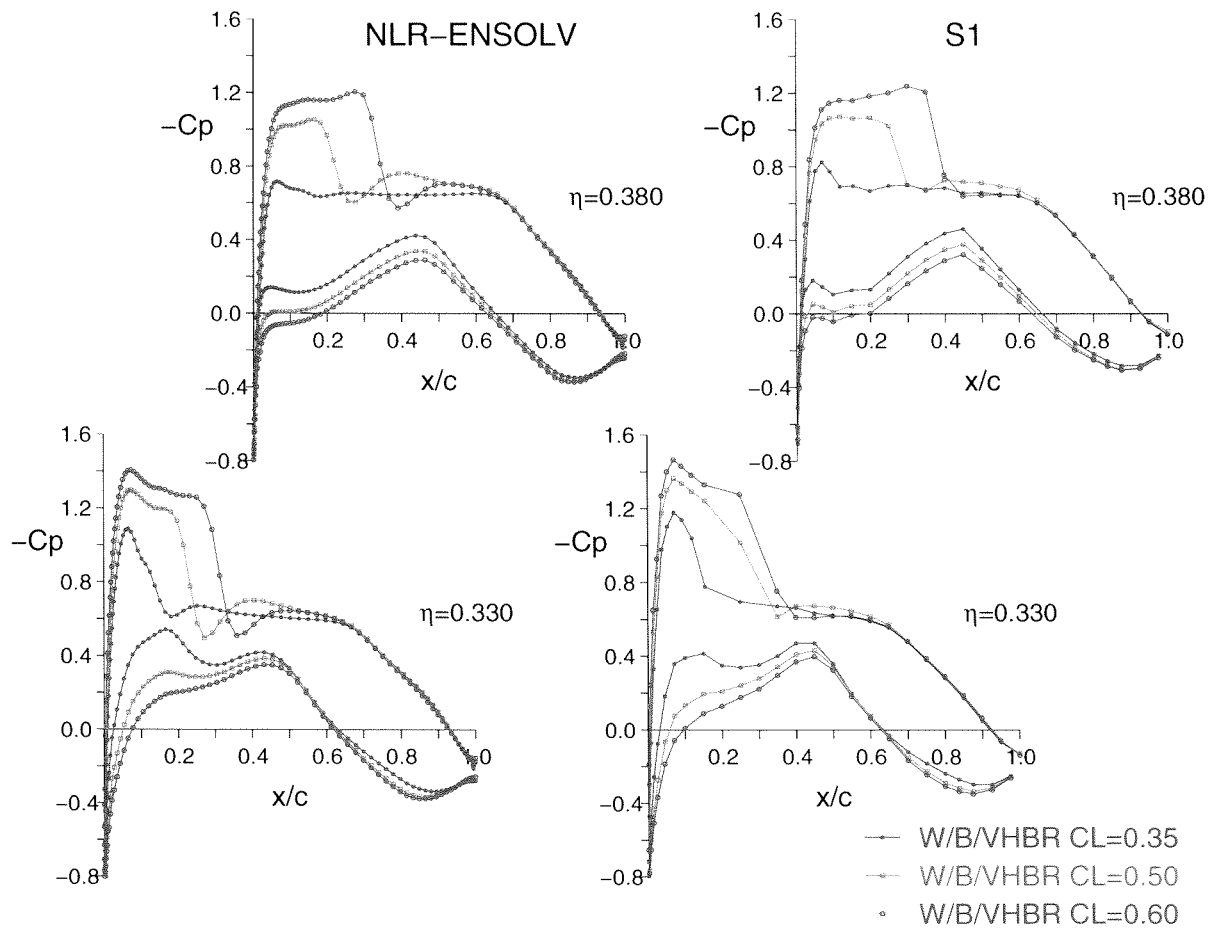


Fig. 15 Influence of lift coefficient variation on wing pressure distribution ($Mach=0.75$, $FPR=2.09$, $Re=4.3M$, S1-transition).

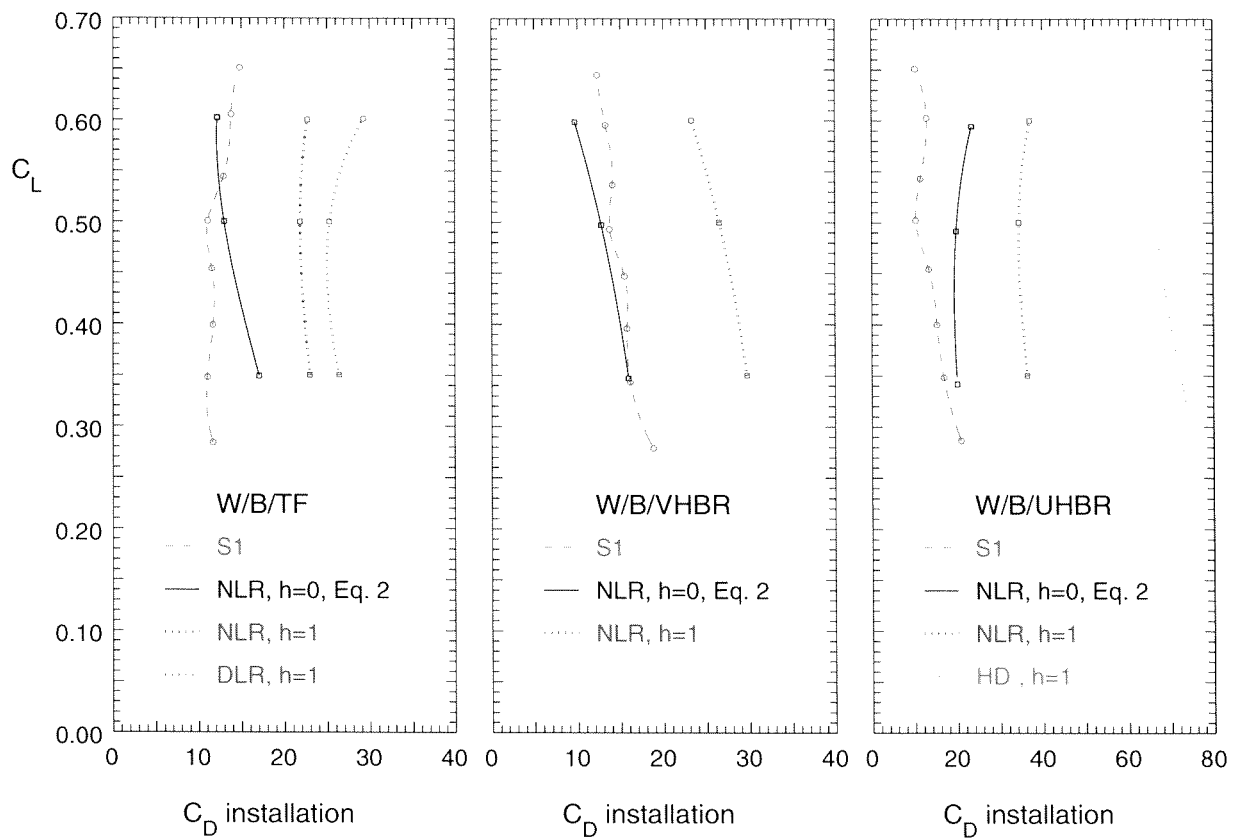


Fig. 16 Installation drag polars for TF, VHBR and UHBR (Mach=0.75, FPR=2.33/2.09/1.72, $Re=4.3M$).

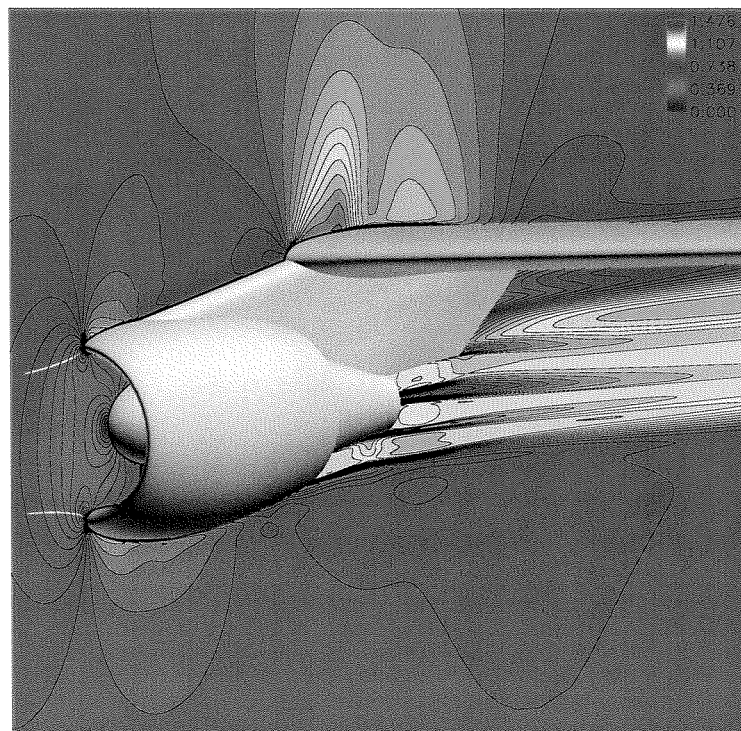
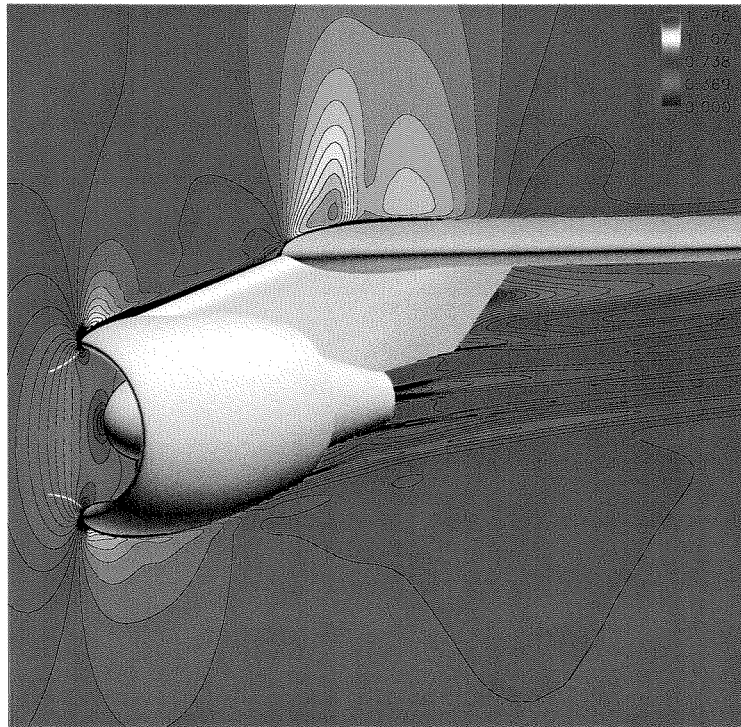


Fig. 17 Wing/Body/TF Mach number distribution for TFN (upper) and SOC (lower) conditions.

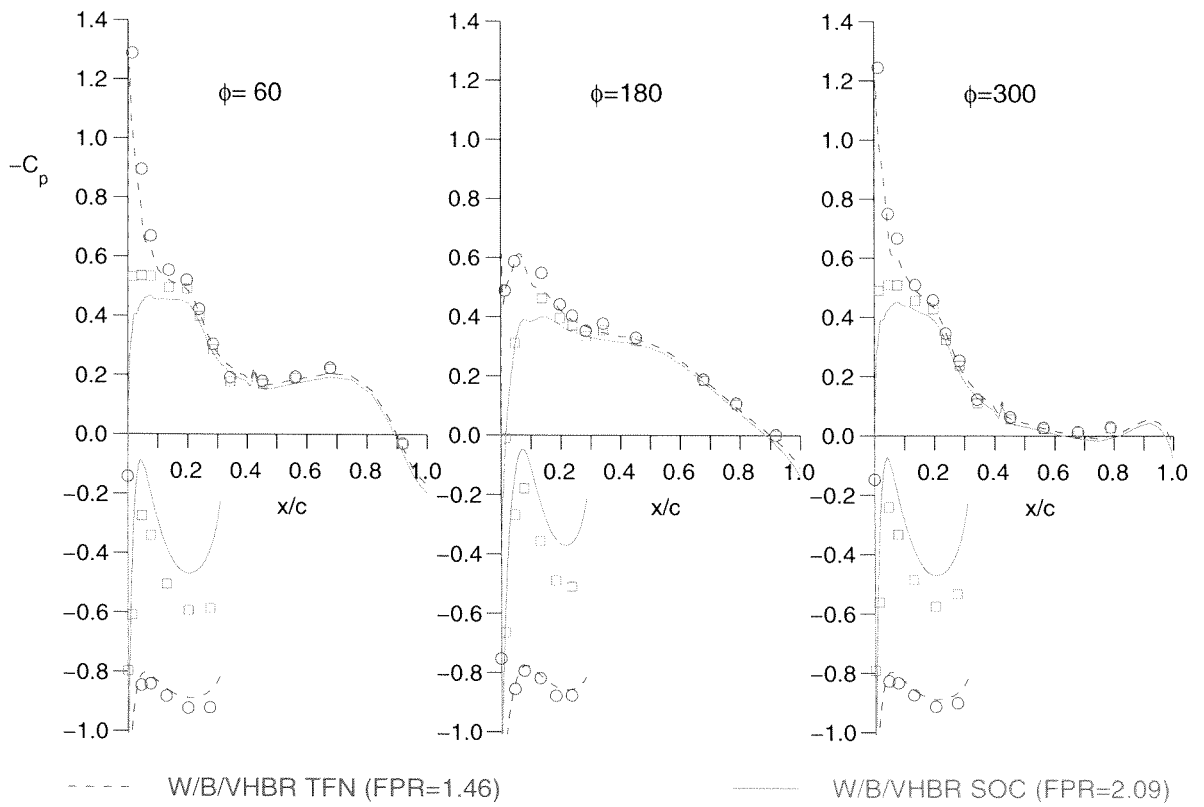


Fig. 18 Influence of fan pressure ratio variation on nacelle pressure distribution, Wing/Body/VHBR (Mach=0.75, $CL=0.50$, $Re=4.3M$, S1-transition).

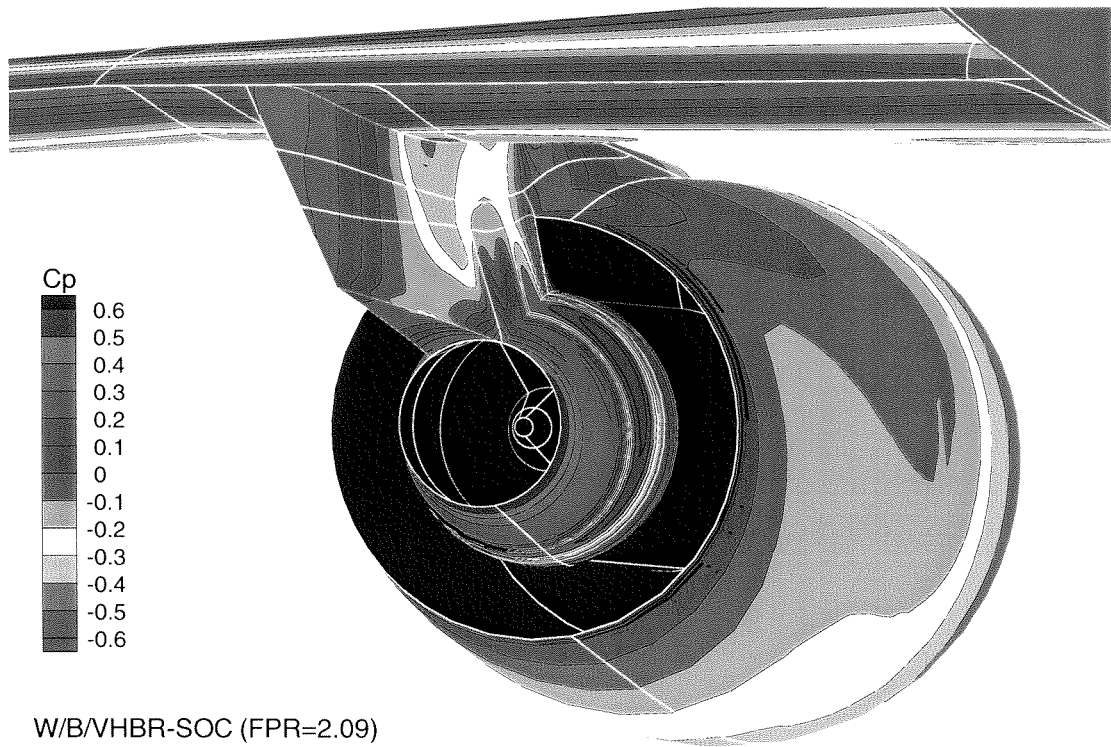
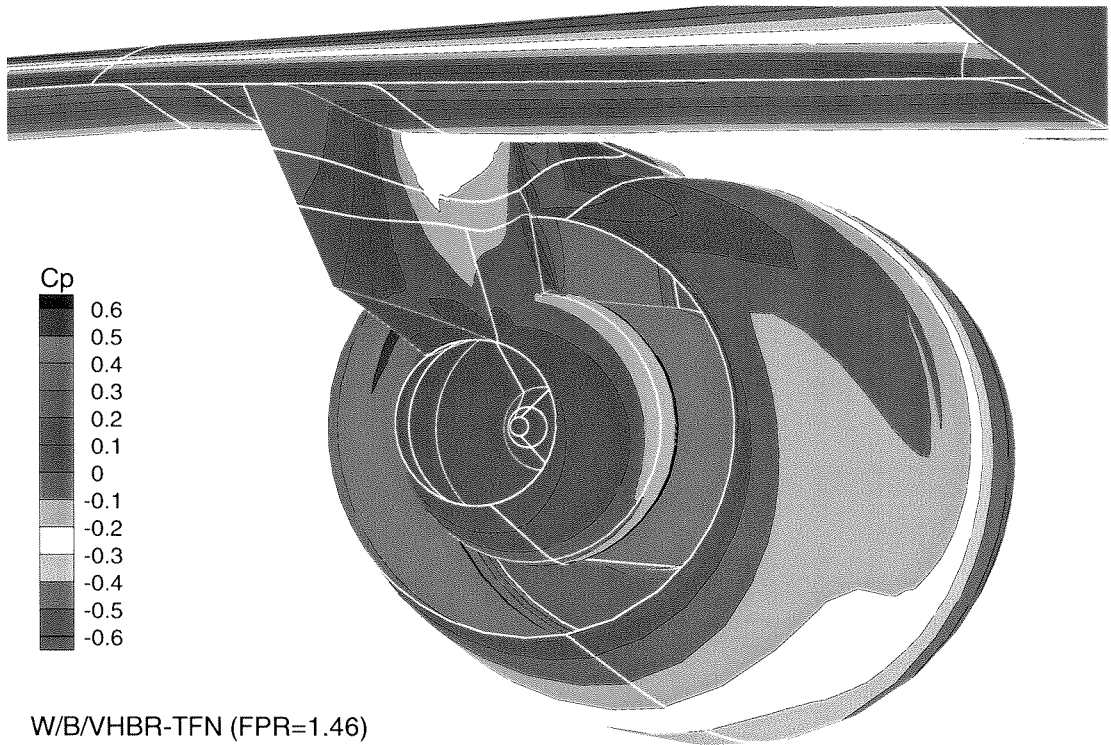


Fig. 19 Influence of fan pressure ratio on pylon and lower wing pressure, Wing/Body/VHBR (Mach=0.75, $CL=0.50$, $Re=4.3M$, S1-transition).

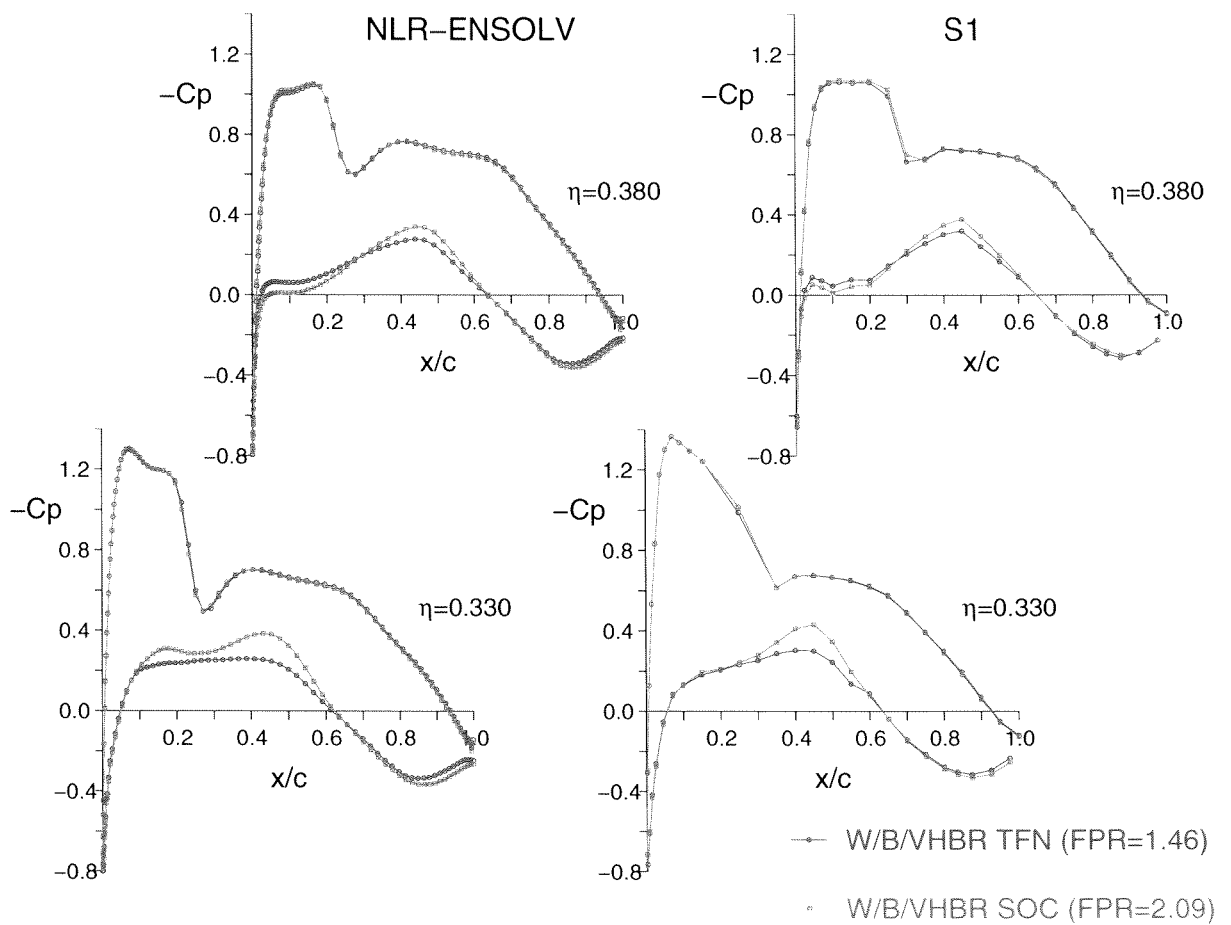


Fig. 20 Influence of fan pressure ratio variation on wing pressure distribution, Wing/Body/VHBR (Mach=0.75, $CL=0.50$, $Re=4.3M$, S1-transition).



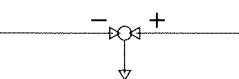
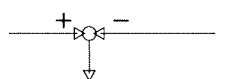
| | | installation drag | | power effect | | |
|------|-----------|-------------------|---|------------------|---|------------------|
| | | W/B |  | W/B/P/N -SOC- |  | W/B/P/N -TFN- |
| TF | S1 | 309 | 14 | 323 | -4 | 327 |
| | DLR (h=0) | 237 | 16 | 253 | -26 | 279 |
| VHBR | S1 | 309 | 13 | 322 | -4 | 326 |
| | NLR (h=0) | 253 | 12 | 265 | 2 | 263 |
| | DLR (h=0) | 237 | 13 | 250 | -3 | 253 |
| UHBR | S1 | 309 | 13 | 322 | -10 | 332 |
| | HD (h=1) | 346 | 67 | 413 | 5 | 408 |

Fig. 21 Summary of installation drag and power effect numbers in drag counts, (Mach=0.75, CL=0.50, Re=4.3M).

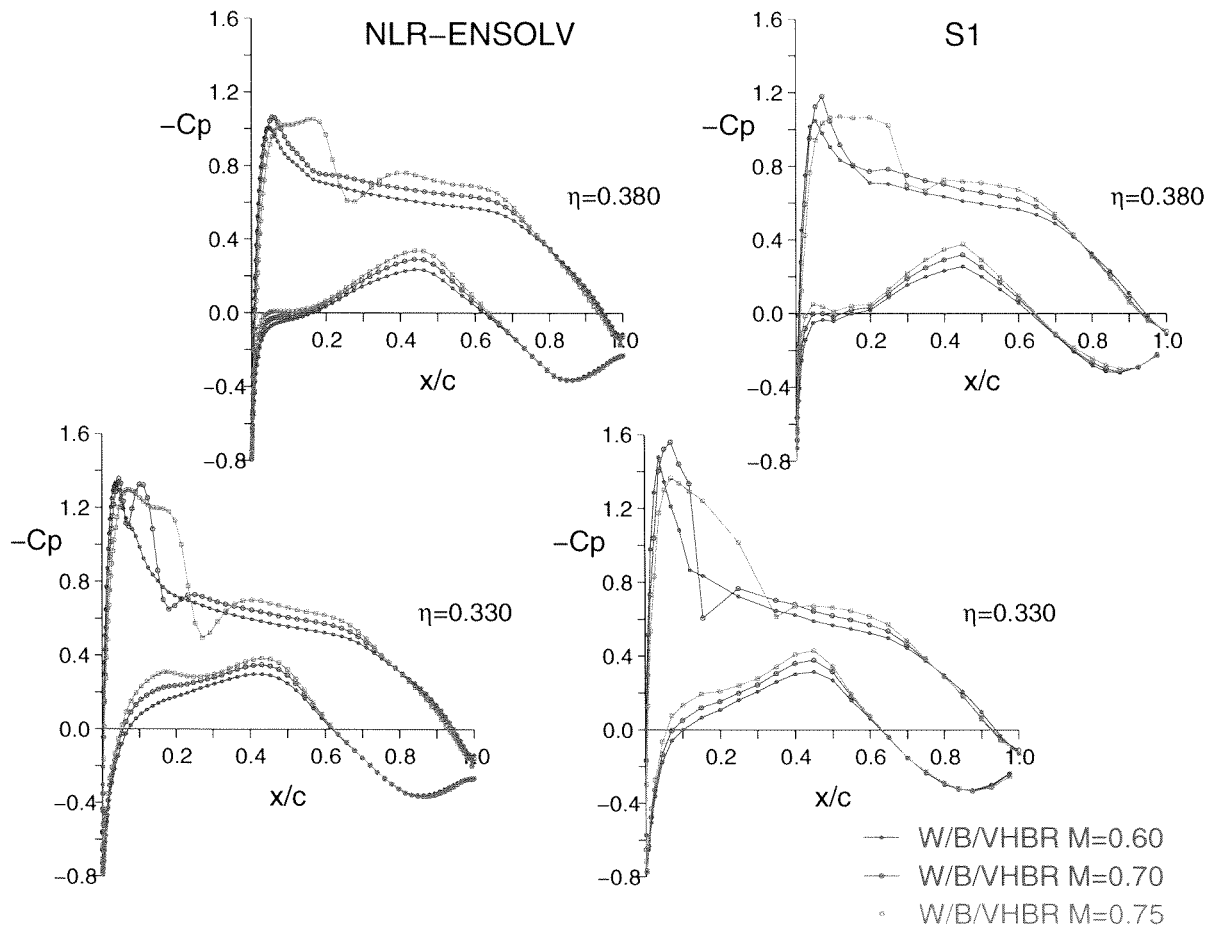


Fig. 22 Influence of Mach number variation on wing pressure distribution, Wing/Body/VHBR ($CL=0.50$, $FPR=1.80/1.99/2.09$, $Re=4.3M$, S1-transition).

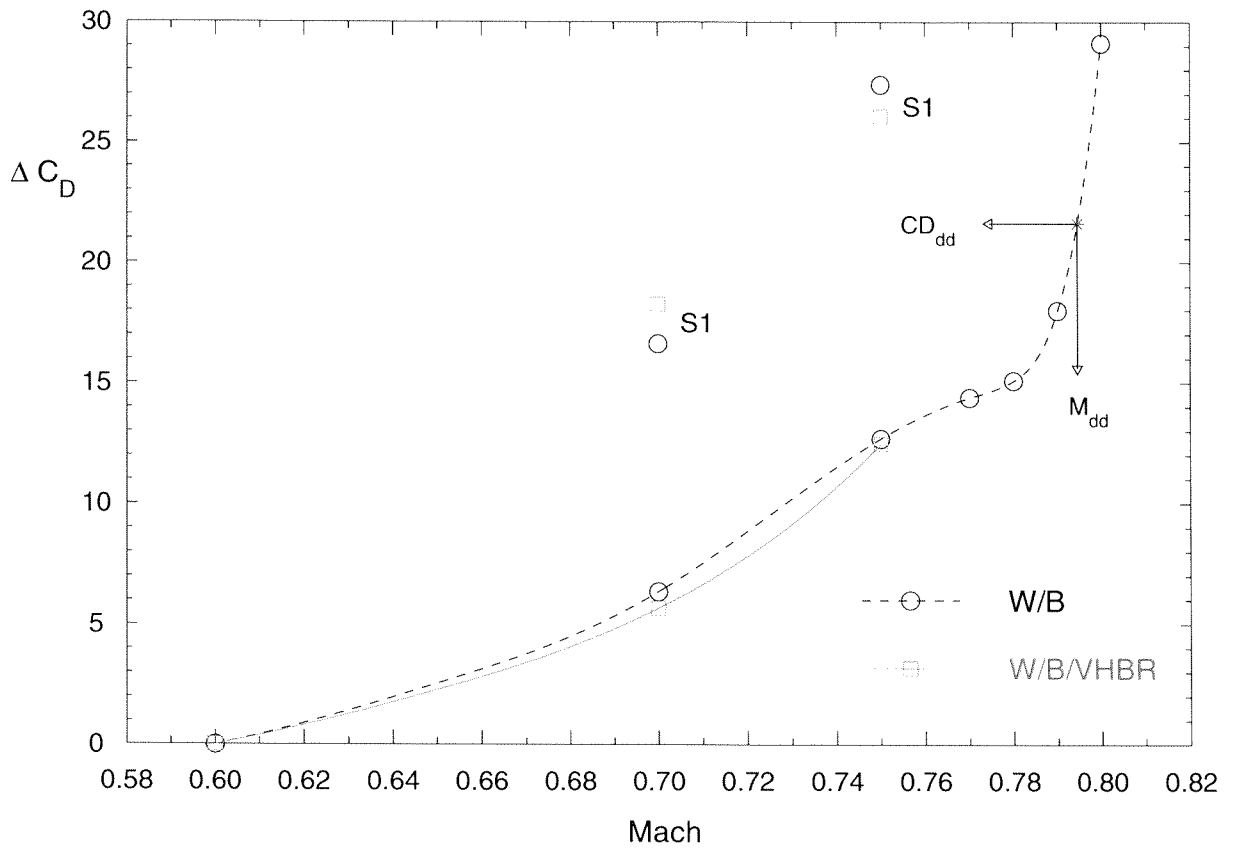


Fig. 23 Transonic drag rise as function of freestream Mach number, Wing/Body and Wing/Body/VHBR configurations ($CL=0.50$, $FPR=1.80/1.99/2.09$, $Re=4.3M$, S1-transition).